Kaustuv Banerjee

Non linear behaviour of three terminal graphene devices

School of Electrical Engineering

Thesis submitted for examination for the degree of Master of Science in Technology.

Espoo May 27, 2011

Thesis supervisor:

Prof. Harri Lipsanen

Thesis instructor:

M.Sc. (Tech.) Wonjae Kim

A" Aalto University
School of Electrical Engineering

AALTO UNIVERSITY
SCHOOL OF ELECTRICAL ENGINEERING

ABSTRACT OF THE
MASTER'S THESIS

Author: Kaustuv Banerjee

Title: Non linear behaviour of three terminal graphene devices

Date: May 27, 2011 Language: English Number of pages:9+65

Department of Micro and Nanosciences

Professorship: Nanotechnology Code: S-104

Supervisor: Prof. Harri Lipsanen

Instructor: M.Sc. (Tech.) Wonjae Kim

Graphene, a 2D allotrope of carbon, has, since its synthesis in 2004, taken the world of physicists by storm. By virtue of its unique energy spectrum graphene exhibit many unique electronic properties - ultra high mobility of charge carriers and ambipolar effect are two of the most important ones. Three terminal ballistic junctions (TBJ), a new class of device, which has in past showed a host of novel non linear electrical properties when fabricated out of semiconductor heterostructure, can be used to form active devices out of graphene that contravene the latter's gapless nature.
In this thesis three terminal junctions were fabricated on both mono- and bi-layer graphene. When operated in a push-pull configuration at room temperature both of them displayed near parabolic voltage and current output. Due to the ambipolar effect of graphene the nature of the output curves could be tuned with a back gate voltage. It was observed that the output curves tend to bend upward for operation in the electron transport regime and downward in the hole transport regime. More over, the output curves became progressively more non linear as the back gate voltage drove the system deeper into either of these regimes. Both of these observations were in direct opposition to the data published in earlier literatures. The voltage rectification of the devices were found out to be $\sim 5\%$.
With clearer theoretical understanding of the mechanism and better fabrication strategies it is hoped that three terminal graphene junctions can be used to make rectifiers, frequency multipliers and logic gates capable of performing at high speed and low power.

Keywords: Graphene, ballistic transport, three-terminal junctions, non-linear electrical property, nano-electronics

Acknowledgment

This thesis was carried out in the Nanotechnology Group of the Department of Micro- and Nanosciences in the Aalto University School of Science of Technology, formerly known as the Helsinki University of Technology.

I am sincerely thankful to Prof. Harri Lipsanen for giving me the opportunity of working with graphene. This work would not have been possible without the able guidance and excellent experimental abilities of my thesis instructor M.Sc. (Tech.) Wonjae Kim - words fall short in expressing my gratitude for him. He was patient enough to teach me the operation of the entire gamut of instruments used in this thesis and kind enough to lend one of his samples for measurement when mine failed. I am also thankful to the personels of Micronova for providing me with the training for various instruments I used during the course of this work.

A warm word of thanks to my friends, here, there and everywhere, for their untiring effort in making the passage of time feel relative, and less tiresome. Finally, I would like to express my deepest gratitude to my family for being there throughout this endeavour.

Espoo, May 27, 2011

Kaustuv Banerjee

Contents

Abstract **ii**

Acknowledgment **iii**

Contents **iv**

Symbols and abbreviations **vi**

List of figures **viii**

1 Introduction **1**

1.1 Background 1
1.2 Scope of the Thesis 2
1.3 Outline of the Thesis 3

2 Theory **4**

2.1 Graphene 4
2.1.1 Electronic properties of graphene 5
2.1.2 Physical properties of graphene 10
2.1.3 Applications of graphene 11
2.2 Ballistic transport 12
2.3 Three terminal ballistic junctions 13
2.3.1 Principle of operation 13
2.3.2 Implementation 15
2.3.3 Applications 18

3 Experimental methods **20**

3.1 Synthesis of graphene 20
3.2 Characterisation of graphene 22
3.2.1 Optical microscopy 22
3.2.2 Atomic force microscopy 24
3.2.3 Raman spectroscopy 25
3.3 Fabrication on graphene 27
3.3.1 Nanolithography 28

3.3.2 Metalisation . . . 30
3.3.3 Etching . . . 31

4 Fabrication techniques and results **34**
4.1 Sample preparation . . . 34
4.2 Sample characterisation . . . 35
4.3 Fabrication on sample . . . 37

5 Measurement and discussion **44**
5.1 Measurement results . . . 44
5.2 Discussion . . . 54
5.3 Future outlook . . . 56

6 Conclusion **57**

Bibliography **59**

Symbols and abbreviations

Symbols

Fundamental constants

c	speed of light in free space	2.9×10^{8} m/s
e	electronic charge	1.6×10^{-19} C
h	Planck's constant	6.626×10^{-34} Js
$\hbar$	reduced Planck's constant	1.055×10^{-34} Js
m	free electron mass	9.11×10^{-31} kg
ϵ_0	permttivity of free space	8.854×10^{-12} F/m

Other symbols used

α	non linearity coefficient
ϵ_d	dielectric constant
μ_c	mobility
μ	electrochemical potential
ρ	resistivity
τ_m	relaxation time
σ	Pauli matrix
a	lattice constant
C	capacitance
E	energy
E_F	Fermi level
$f(E)$	Fermi-Dirac distribution
G	conductance, or, conductivity
$\mathcal{H}$	Hamiltonian
I	current
$\mathbf{k}$	wave vector
$\mathbf{K}$	Dirac point
L_m	mean free path
n	carrier concentration
$\mathcal{O}$	asymptotic notation
$\mathbf{q}$	momentum vector
t	nearest neighbour hopping energy
$t_\perp$	interlayer hopping energy
t_d	dielectric thickness
T	transmissivity
V	voltage
V_{BG}	back gate voltage
v_F	Fermi velocity

Abbreviations

2D	two dimensional
3D	three dimensional
AFM	atomic force microscopy
BLG	bilayer graphene
CNP	charge neutrality point
DIW	deionised water
DOS	density of states
EBL	electron beam lithography
FET	field effect transistor
FIB	focused ion beam lithography
FLG	few-layer graphene
GNR	graphene nano-ribbon
HEMT	high electron mobility transistor
IPA	iso-propyl alcohol
MCP	minimum conductance plateau
MIBK	methyl isobutyl ketone
MLG	monolayer graphene
MMA	methyl methacrylate
PMMA	polymethyl methacrylate
RIE	reactive ion etching
SEM	scanning electron microscope
TBJ	three terminal ballistic junction
YBS	Y-branch switch

List of Figures

1 2D graphene acts as building material for graphitic materials of other dimension . . . 4
2 Electronic structure of MLG . . . 7
3 Electronic structure of BLG . . . 8
4 Ambipolar electric field effect in graphene and effect of doping . . . 9
5 Schematic representation of a TBJ with adiabatic boundaries . . . 13
6 Voltage output from central branch of a TBJ . . . 15
7 Non linear operation of a practical TBJ device . . . 16
8 TBJ fabricated from graphene and electrical measurements . . . 17
9 Schematic explaining change of sign of output voltage due to back-gate voltage in a graphene TBJ . . . 17
10 Frequency multiplier using TBJ . . . 18
11 Micromechanical cleavage of graphene by scotch-tape method . . . 21
12 Contrast of MLG as a function of wavelength and thickness of SiO_2 substrate . . . 23
13 Practical effect of dioxide thickness and wavelength used on visibility of graphene . . . 23
14 Schematic of Atomic Force Microscope . . . 24
15 AFM images of graphene . . . 25
16 Schematic of a modern day Raman spectrometer . . . 26
17 Comparison of Raman spectra for MLG, BLG and bulk graphite . . . 27
18 Progression of 2D band of graphene layers . . . 27
19 Block diagram of an Electron Beam Lithography tool . . . 29
20 Schematic for electron beam evaporation technique for metal deposition 31
21 Lift-off technique of metalisation . . . 32
22 Schematic of a parallel plate reactive ion etching chamber . . . 32
23 Optical microscope image of graphene flakes on dioxide layer of different thickness . . . 34
24 Obtained AFM image of graphene flakes . . . 36
25 Obtained Raman signature of different graphene flakes with varying number of layers . . . 36
26 Spectral deconvolution of 2D band of the Raman signature of a graphene flake . . . 37

27 Representative diagram of Y-branch fabricated on graphene 38

28 AFM image of contaminations on a graphene flake after FIB-assisted Pt deposition 39

29 SEM image of Ti/Au metal lines deposited on a MLG flake 40

30 SEM image of the MLG flake in the previous figure after etching . . . 41

31 SEM image of a BLG flake after etching for 90 seconds 41

32 SEM image of the BLG flake in the previous figure after further 30 seconds of etching 42

33 Raman signature of a MLG flake before and after annealing 42

34 Schematic of measurement setup 44

35 I_C vs V_{BG} graphs for MLG and BLG device 45

36 I_C vs E_F graphs for MLG and BLG device 46

37 Output curve for BLG device in push-pull configuration 47

38 Analysis of voltage output data from BLG 48

39 Output curve for MLG device in push-pull configuration 50

40 Analysis of voltage output data from MLG 51

41 Study of effect of asymmetrical bias on MLG and BLG device 52

42 I_L vs V_L curve obtained during push-pull measurements on BLG and MLG device 52

43 Current rectification in BLG and MLG device under push-pull configuration 53

1 Introduction

1.1 Background

The last half century has seen some rapid technological progresses being made by human civilisation. From harnessing power from the nucleus of atoms, to conquering the deep recesses of space, we have made major advances in all fields of technology. However in no discipline has the progress been as rapid as in the field of electronics - bulky ENIACs of yesteryears have been replaced by hand-held palm-tops, huge volumes of magnetic tape have been replaced by miniature discs. This rapid advancement has been made possible by the ability of physicists and engineers to process and store information in an ever-shrinking network of circuits. However, with the ever-expanding volume of information challenging the very physical limit of semiconductor based devices, which have been the workhorse of this electronic age, the information age may die a premature death. It is slightly ironical that this eventuality had been predicted, though not directly, by Intel co-founder Gordon E. Moore [1] some 40 years back.

However, graphene, a truly two dimensional atomic thick layer of isolated carbon crystal, might save us from this eventuality. Soon after its discovery in 2004 [2], numerous experiments have revealed the exceptional physical properties of graphene that are not found in any other material (for a review of such experiments please refer [3, 4, 5, 6]). It is simultaneously the thinnest and the strongest material known to mankind. It is the best known conductor of heat and electricity, is impermeable to gases and is capable of detecting adsorption of a single molecule.

By virtue of the excellent crystal quality of graphene, even those formed by a very "crude" method employing scotch tapes and ordinary graphite, charge carriers in it travel at a speed of 10^6 m/s. In effect, these charge carriers have zero effective mass, and under the right condition, can travel for micrometers without scattering. While such "ballistic transport" of electrons have been achieved previously in semiconductor heterostructure, the process of growing such crystals is expensive and cumbersome. Electron states in graphene are described by a Dirac-like equation, rather than the more familiar Schrödinger equation. This allows for investigation of quantum relativistic phenomenon in a convenient bench-top experimental setup.

The electrons in graphene obey a linear dispersion relation; the resulting energy spectrum is conical in shape. Hence, graphene behaves like a gapless semiconductor.

The obvious advantage of this property is the so called ambipolar electric field effect - charge carriers in graphene can be tuned continuously between electrons and holes in high concentration using an external electric field. Additionally, graphene exhibits extremely high carrier mobility, even under high carrier concentration and at room temperature. These properties has prompted it to be taken as a serious contender for being the successor, if not the replacement, of silicon as the *materia prima* of the electronics industry. However, experimental studies on graphene is still in its infancy and there are lot of issues to be solved before graphene can pose a serious threat to silicon in the semiconductor industry.

One of the primary disadvantages of the gapless nature of graphene is the very low on-off ratios obtained in graphene FETs. In fact conventional design to produce diodes and transistors might not be possible on graphene. A new class of nano-scale devices based on conventional Y-branch switches exploiting the ballistic transport of electrons in a material, the three-terminal ballistic junction (TBJ) might just provide the answer. Initial theoretical modeling based on ballistic transport in such three terminal devices indicated strong non linear output and was predicted for use as rectifiers, frequency multipliers and logic gates [7]. Further studies has extended the non linear behaviour to devices with diffusive transport. Though, there has been a fair share of study done on TBJ devices based on semiconductor heterostructure, till date there has only been one instance of investigation of graphene based three terminal device [8]. This leaves the opportunity of studying three terminal graphene junction in greater detail.

1.2 Scope of the Thesis

The scope of this thesis was the fabrication and electrical characterisation of nano-scaled, three terminal junction devices on graphene. This entailed, first and foremost, synthesising graphene using the "scotch-tape" method (to be discussed in Sec. 3.1). The second step was to identify mono and bi-layer graphene (these terms have been defined in Sec. 2.1) using a combination of optical microscopy, atomic force microscopy and Raman spectroscopy. This was followed by fabrication of nano scaled Y-shaped structure on both mono- and bi-layer graphene; additional metallic structures were fabricated to aid the electrical characterisation of the device. Though the resulting device can be operated in many configuration, the one chosen for this thesis was the so-called push-pull configuration where equal but opposite voltage is applied to the left and right branch of the Y-shaped device and the output

is detected at the central branch.

Room temperature electrical characterisation of the devices revealed a non linear voltage and current output; when plotted against the input, the curve for the output data was found out to be nearly parabolic, albeit not about the x-axis. Furthermore, it was observed that the application of a back-gate voltage changes the nature of the output curve. When the back-gate voltage is such that electrons are the majority carriers in graphene, the output voltage tends to bend upward. It tends to bend downward when the back-gate voltage causes the majority carriers to be holes. In addition to this, increasing the magnitude of the back-gate voltage in either of these regimes causes the output to become progressively more non linear.

1.3 Outline of the Thesis

The rest of thesis is organised in the following order. Chapter 2 gives a theoretical background of graphene and three terminal junction. It includes the definition of graphene as well as its types, followed by a foray into graphene's fascinating electronic and physical properties and their possible applications. The principle of operation of three terminal ballistic junction devices is discussed along with practical implementations and applications so far. Chapter 3 turns the discussion into the various approaches toward realising such a structure in graphene. Various ways of synthesising graphene and identifying the number of layers in it are discussed. Forming a practical device on graphene would require shaping the flake as well as drawing metal contacts to it - nanolithographic and microfabrication techniques that can be used to do so is outlined in this chapter. Chapter 4 gives a step-by-step description of the preparation of the three terminal device onto synthesised and isolated graphene flakes as was done in this thesis. The results obtained at each step of synthesis, characterisation and fabrication of graphene is displayed. Chapter 5 is devoted to electrical characterisation of the obtained device. It gives the measurement results along with analysis of the data and finally analysis of the output in comparison with result published in earlier literatures. Chapter 6 draws a conclusion by giving a brief summary of the entire process.

2 Theory

2.1 Graphene

Graphene, by definition, is a flat monolayer of carbon atoms tightly packed into a two-dimensional honeycomb lattice. Conceptually it can be thought of as a benzene ring stripped of its hydrogen atoms. It acts as the basic building block for graphitic materials of all other dimensionality as seen in Fig. 1. Theoretically, graphene, or "2D graphite" was studied closely over the years and has been widely used to describe properties of other carbon-based material over the years. Ironically however, in spite of being widely studied, it eluded any experimental observation. Numerous attempts to synthesise a stable form of this two-dimensional atomic crystal failed, giving rise to speculations that it is no more than an "academic" material [4].

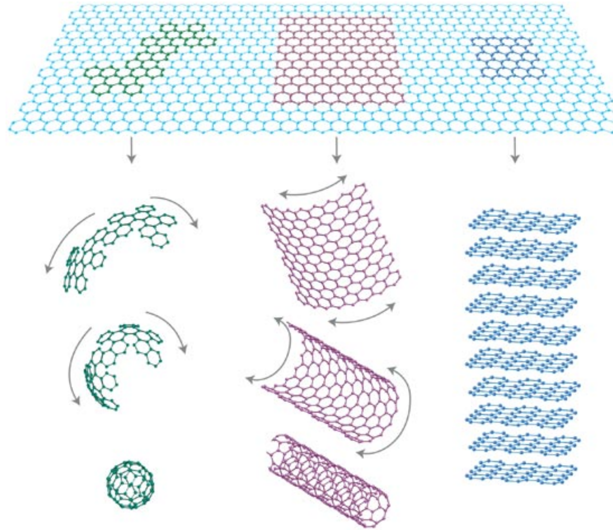

Figure 1: *Graphene is a 2D, planar, hexagonal arrangement of carbon atoms that can be wrapped into 0D buckyballs, rolled into 1D nanotubes or stacked into 3D graphite [4]*

Incidentally, the very fact that two dimensional atomic crystal can exist stably under ambient conditions contravene quite a few theoretical predictions [3]. More than 70 years ago, the eminent physicist Landau argued that strictly 2D crystals were thermodynamically unstable and hence could not exist, an argument that was later extended by Mermin and henceforth, strongly supported by many experimental observations. An absence of long-range order in 2D, a large perimeter-to-surface ratio and a rapid decrease of melting temperature with decreasing thickness were cited as reasons for instability (in the form of segregation into islands or

decomposition) of layers of true atomic thickness. Atomic monolayers have so far been known only to exist as an integral part of a larger 3D structure (e.g. those formed by epitaxial growth).

However, in 2004 a group of physicists led by Andre Geim and Kostya Novoselov used a novel approach to obtain graphene that bypassed most of the problems of thermodynamic instability mentioned earlier. They started with graphite and extracted as single sheet of atoms, i.e. graphene, using a technique called micro-mechanical cleaving [2] (the technique will be explained in greater details in Section 3.1). This anomalous existence of the atomic monolayer was reconciled to earlier, contradictory, theoretical predictions by positing that 2D crystals become intrinsically stable by exhibiting "metastable quenching" and "3D warping" [4]. Importantly, the graphene crystals thus obtained exhibit both long range continuity as well as high crystal quality; this resulted in enormous experimental activities to demonstrate and further the many wonderful physical and electronic properties that were predicted of this novel material. Some of the major properties will be discussed in the next two sections with a short, and by no means exhaustive, discussion on possible applications of graphene.

Before proceeding further it would be instructive to explain how 2D crystals are defined in the case of graphene from an experimental point of view. Digressing from the obvious theoretical viewpoint of treating the monolayer as 2D and hundred or more layers as essentially a thin film of 3D material, it would be helpful to choose a suitable "transition point" from 2D to 3D. It has been observed that the electronic structure of stacks of graphene rapidly evolve with number of layers, approaching the 3D limit of graphite at ten layers. Additionally, only graphene and to some extent its bi-layer has simple electronic spectra. This has resulted in single-, double- and few- (3 to 10) layer graphitic material to be distinguished as three different types of "graphene" - monolayer (MLG), bilayer (BLG) and few-layer (FLG) graphene [4]. Pedantic aside, such division is also sensible from an experimental point of view.

2.1.1 Electronic properties of graphene

The structural flexibility and fascinating electronic property of graphene results from its crystal structure. The carbon atoms in a monolayer of graphene are sp^2 hybridised leading to formation of a trigonal planar structure with σ bonds between adjacent atoms. The unaffected p-orbital, which lies perpendicular to the planar structure forms a loose π bond with similar orbital of neighbouring atoms. The

resultant lattice structure consisting of two equivalent carbon sublattices is shown in Fig. 2a; it can alternately be viewed as a triangular lattice vector with a basis of two atoms per unit cell. The lattice vectors can be written as $\mathbf{a_1} = a/2(3, \sqrt{3})$ and $\mathbf{a_2} = a/2(3, -\sqrt{3})$, where $a \approx 1.42$ Å is the carbon-carbon distance. It is worth taking a note of the two points $\mathbf{K}$ and $\mathbf{K'}$ located at the corner of the Brillouin zone - these are called Dirac points and are of paramount importance to the electronic structure of MLG, as will be seen here. Their position in momentum space is given by:

$$\mathbf{K} = \frac{2\pi}{3a}\left(1, \frac{1}{\sqrt{3}}\right), \qquad \mathbf{K'} = \frac{2\pi}{3a}\left(1, -\frac{1}{\sqrt{3}}\right) \tag{1}$$

Under the nearest neighbour, tight-binding approach [9] the electronic band structure of MLG can be expressed as:

$$E_{\pm}(\mathbf{k}) = \pm t\sqrt{3 + 2\cos(\sqrt{3}k_y a) + 4\cos\left(\frac{\sqrt{3}}{2}k_y a\right)\cos\left(\frac{3}{2}k_x a\right)} \tag{2}$$

where, $t \approx 2.8$ eV is the nearest neighbour hopping energy and $\mathbf{k}$ is the wave vector. The plus sign applies to upper (π) and the minus sign to lower (π^*) band. When Eq. 2 is expanded close to the $\mathbf{K}$ (or $\mathbf{K'}$) vector, as given in Eq. 1, the following equation is obtained [10]:

$$E_{\pm}(\mathbf{q}) = \pm\hbar v_F|\mathbf{q}| + \mathcal{O}((q/K)^2) \tag{3}$$

where, $\mathbf{q}$ is the momentum measured relatively to Dirac points and $v_F = c/300 = 10^6$ m/s is the Fermi velocity.

The band structure with a detailed view near Dirac points is shown in Fig. 2b and it clearly shows a conical band structure with the valence and conduction band touching at Dirac points making MLG a zero gap semiconductor. Incidentally, the linear energy dispersion in Eq. 3 resembles that of ultra-relativistic particles, more specifically that of massless Dirac fermions traveling with the speed of v_F. The interaction of electrons with the periodic potential of graphene's honeycomb lattice give rise to new massless, charge-carrying quasi-particles with a chiral pseudospin index. Under the long wavelength, low energy approximation they can be described by the Dirac like Hamiltonian [10]:

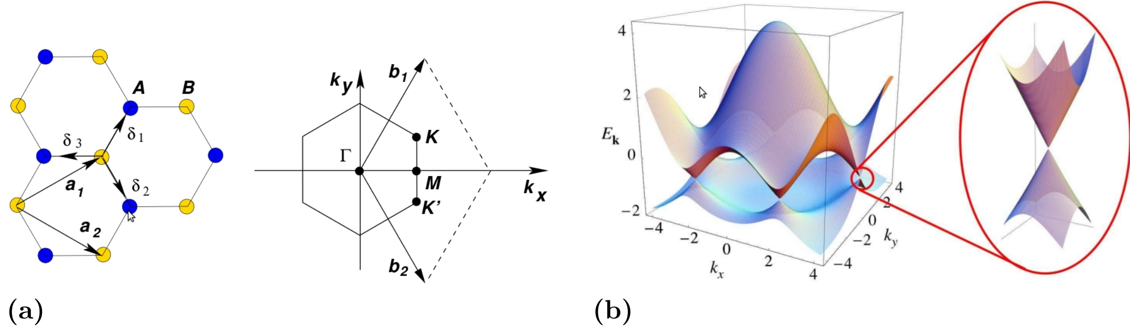

Figure 2: *a. Lattice structure of MLG and corresponding Brillouin zone; b. Energy spectrum of MLG with an enlargement close to Dirac point [10]*

$$\mathcal{H} = \hbar v_F \begin{pmatrix} 0 & k_x - ik_y \\ k_x + ik_y & 0 \end{pmatrix} = \hbar v_F \sigma.\mathbf{k} \tag{4}$$

Bilayer graphene, with two carbon monolayers (inter-layer separation of 0.3 nm) weakly coupled by electron hopping between the layers, has a totally different electronic structure. Though the charge carriers in BLG are still chiral, the energy dispersion is no longer Dirac-like. Considering the so-called A-B stacking of layers (Fig. 3a), the low energy, long wavelength dispersion is given by the relation [11]:

$$E_{\pm}(\mathbf{q}) = \sqrt{V^2 + \hbar^2 v_F^2 q^2 + t_{\perp}^2/2 \pm (4V^2\hbar^2 v_F^2 q^2 + t_{\perp}^2 \hbar^2 v_F^2 q^2 + t_{\perp}^4/4)^{1/2}} \tag{5}$$

where, $t_{\perp} \approx 0.4$ eV is the effective interlayer hopping energy and V is shift in inter-layer electro-chemical potential due to external voltage and/or electric charge induced on bilayer. From the above relation it can be deduced that BLG has an effective bandgap $\Delta_g \approx V\sqrt{t_{\perp}^2/(t_{\perp}^2 + V^2)}$ for non-zero V. For zero applied external bias, however, BLG appears to be a gapless semiconductor with a parabolic dispersion relation $E_{\pm}(q) \approx \hbar^2 q^2/(2m^*)$, with $m^* \approx 0.03 \times m$. For high values of q ($\hbar v_F q > t_{\perp}$), corresponding to carrier densities larger than 5×10^{12} cm^{-2}, a linear dispersion relation $E_{\pm}(q) \approx \hbar v_F q$, identical to that of MLG, is obtained. As can be seen in Fig. 3b, the dispersion relation, in-spite of being parabolic maintains the electron-hole symmetry observed in MLG. Beyond bilayer, graphitic system becomes increasingly metallic with increasing number of layers.

Thus, one of the distinguishing properties of graphene, both MLG and BLG, is

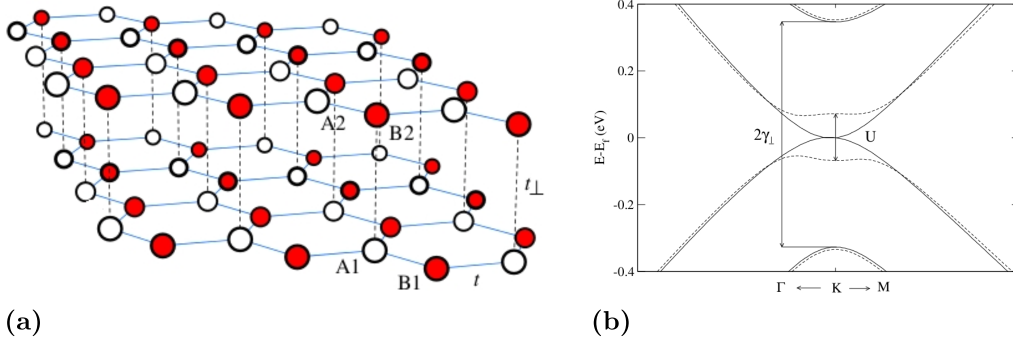

(a) (b)

Figure 3: *a. Lattice structure of BLG with A-B interlayer stacking; b. Energy dispersion relation in BLG with(dashed line) and without(solid line) external potential [12]*

that it is a gapless semiconductor where the nature of carrier changes from hole to electron (and vice versa) at the Dirac point, also known as the charge neutrality point (CNP). An easy way of tapping this ambipolar effect of graphene is offered by tuning the electro-chemical potential (or Fermi level E_F) of the system by applying an external potential. The easiest way to do so is to use a back-gate configuration fashioned as a parallel plate capacitor consisting of silicon and graphene with an intermediate layer of silicon dioxide acting as the dielectric. A finite back gate voltage of V_{bg} applied to silicon layer would induce charge carriers in the graphene layer, the magnitude of concentration of which is given by:

$$|n| = \frac{C|V_{bg}|}{e} + n_Q\left[1 - \sqrt{1 + \frac{C|V_{bg}|}{en_Q}}\right] \tag{6}$$

where, $C = \frac{\epsilon_d \epsilon_0}{t_d}$ is the gate capacitance with t_d being the dielectric thickness and $n_Q = \frac{\pi}{2}(\frac{C\hbar v_F}{e^2})^2$. The second part of the equation arises due to quantum capacitance effects and can be safely ignored for thick oxide layers that are commonly in use. The electrochemical potential of MLG and BLG are associated in different degrees to their respective carrier concentration as [11]:

$$\textbf{MLG:} \qquad |E_F| = \hbar v_f \sqrt{\pi |n|} \tag{7}$$

$$\textbf{BLG:} \qquad |E_F| = \frac{\pi \hbar^2 |n|}{m^*} \tag{8}$$

A positive back-gate voltage ($V_{bg} > 0$) leads to the accumulation of electrons in

graphene ($n < 0$), causing the Fermi level to rise above the Dirac point, into the conduction band ($E_F > 0$), and vice versa. Increasing the magnitude of V_{bg} leads to a linear increase in charge carrier concentration due to an increase in density of states (DOS). Thus, the relation between back-gate voltage and conductivity of graphene is characterised by a high resistivity at $V_{bg} = 0$, with the resistivity falling rapidly on either side, as explained in Fig. 4a.

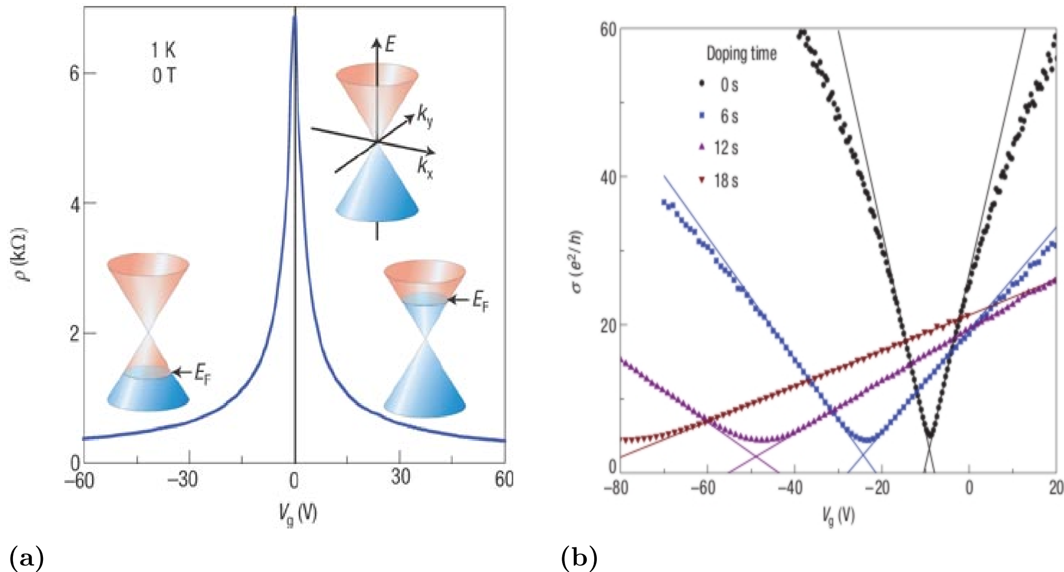

Figure 4: *a. Ambipolar electric field effect in graphene. Inset shows its conical low energy spectrum indicating changes in position of Fermi Energy E_F with changing gate voltage V_g [4]; b. Effect of n-doping of graphene with phosphorus on position of CNP and mobility [13]*

Though this simple model would seem to suggest that the conductivity of graphene should be zero when $E_F = 0$ (i.e. the Fermi level is at Dirac point - with a vanishing DOS at this point, n should be zero too) experiments seem to indicate a finite minimum conductivity of the order of $\sim 4e^2/h$. Further studies have shown that transport in graphene is significantly affected by long-range Coulomb scattering and subsurface charged impurities. Among other things, these factors result in a finite DOS, and hence, a finite charge carrier density at the Dirac point [11, 14]. This transport mechanism has been used to explain the presence of, and to obtain analytical expressions for, the minimum conductivity plateau (MCP) at CNP and dependence of mobility and Dirac point on impurity concentration in graphene [15].

Another remarkable property of graphene is the high mobility μ_c of its charge carriers (as, $\mu_c = 1/\rho n e$, a high μ_c can be inferred from the rapid decrease in

resistivity ρ in Fig. 4a). Mobilities exceeding 15 000 cm^2/Vs has been reported for samples with high degree of impurity, even under ambient conditions [4]. This gave rise to hopes of observing ballistic transport in submicrometre scale - this property and important ramifications thereof will be examined in further detail in Section 2.2. It must be noted that most of this discussion is based on the assumption that E_F is exactly at the Dirac point when $V_{bg} = 0$, i.e., the graphene is *intrinsic* (or, undoped). However, this is more of an equilibrium model; an infinitesimal amount of doping (in the form of impurities or external potential or thermal fluctuation), makes the system *extrinsic* and CNP is reached for some finite V_{bg} - especially at higher temperatures [11]. In addition to shifting the Dirac point, external doping also affects the mobility of sample [13], as can be seen from Fig. 4b.

The material above is a short discourse on the fascinating electronic properties of graphene - for a detailed and comprehensive reference of electronic properties of graphene readers are referred to Ref [10, 11, 14].

2.1.2 Physical properties of graphene

With the plethora of electronic properties of graphene it is but customary to overlook its non-electronic properties. Recent research in this field has revealed graphene's remarkable physical and optical properties, thereby opening up new possibilities with regard to its application.

The first measurement of graphene's mechanical and thermal properties revealed a breaking strength of 42 N/m (it correspond to a Young's modulus of 1.0 TPa and an intrinsic strength of 130 GPa) and a room-temperature thermal conductivity of $\sim$ 5000 W/mK [16]. This makes it the strongest as well as the most conductive man-made material. Graphene has a very high optical transparency (it reflects only $<$ 0.1%of visible light), shows luminescence over a broad spectral range, and, owing to its linear dispersion relation, allows for ultra wideband optical tunability [17]. The chemical properties of graphene, as yet unexplored, promise to open up new fields too - it can adsorb and desorb various atoms and molecules and is impermeable to a variety of gases. The exploration of physical properties of graphene are, as yet, in its nascent stage. It is expected to yield more results with improvement in production method.

2.1.3 Applications of graphene

As with theoretical and experimental work on graphene, a large share of research on application is geared towards graphene based electronics. However, relatively low on-off ratios (limited to less than hundred because of graphene's minimum conductivity) and the fact that graphene remains metallic even at neutrality points act as primary deterrents to progress [4]. Various novel techniques are being conceptualised to circumscribe these difficulties, the most widely used approach being that of the graphene nano-ribbons (GNR). Spatial confinement effects due to the narrow width ($\approx 10 - 20$ nm) of GNR allow a band-gap to be opened for room temperature operation. This ensures semi-conductor like behaviour and FETs constructed of such material have shown an on-off ratio as high as 10^7 at room temperature [18]. The ability to induce and tune the bandgap in BLG using an external electrical field [19] makes it a desirable candidate for electronic applications. Graphene has been used to form ultrahigh-frequency analogue transistors, known as high-electron mobility transistors (HEMT), which have the potential to operate well into tetrahertz frequencies [20]. In spite of the reigning optimism about graphene based electronics, by all indications, it will be some time before they pose a serious challenge to the present silicon based market.

Meanwhile it would be instructive to check its usability in other fields. Graphene powder is shown to be excellent, low-cost filler for compound materials [21]; additionally, by virtue of its large surface-to-volume ratio and high conductivity it can be used in batteries, supercapacitors and field emitters [5]. Graphene based gas sensors capable of detecting single molecule have been demonstrated [22]. Given its lightness and stiffness graphene could be an excellent choice for nano-electro-mechanical systems. Already, membranes with a quality factors of ~ 100 at 100 MHz frequencies have been demonstrated [23]. Graphene has also been used in a wide range of optical devices like touch-screens, LED's, solar cells, etc. [17]

However, given the lack of direct electronic application of graphene, the opportunity remains to investigate into novel devices that utilise the ultra-fast mobility of graphene. The next section will focus on the most direct implication of the high mobility of charge carriers in graphene - ballistic transport.

2.2 Ballistic transport

The passage of electron through any medium subjected to an external electric field is affected by scattering from one or more localised non-uniformities (e.g impurities, defects, surface effects, etc.) forcing it to deviate from a straight trajectory. Ballistic transport of electrons, in its simplest term, is said to happen when the trajectory is unaffected by scattering, except those due to device boundary. It is observed to occur when the dimension of the medium is smaller than the characteristic scattering lengths (viz. the mean free path, the phase relaxation length and the Fermi wavelength) of electron in that medium [24]. The electrical conductance G of a ballistic conductor is quantised (at low temperatures) and is expressed by the Landauer formula $G = \frac{2e^2}{h}N$ (where, N is the total number of occupied transverse quantum confinement modes in the channel) unlike the more familiar Ohm's Law. In recent years, ballistic transport of electrons has been observed in certain semiconducting material viz. GaAs, GaAs/AlGaAs in low temperature and $Ga_{0.25}In_{0.75}As/InP$ at room temperature. Electron mobilities as high as 15 000 cm^2/Vs at room temperature and 100 000 cm^2/Vs at 77 K has been observed in these materials [25].

Graphene, as has been explained earlier, has a very high charge carrier mobility. This indicates high relaxation time τ_m (since, $\tau_m = \frac{\mu_c m}{e}$) and large mean free path L_m (since, $L_m = \tau_m v_F$), and hence, a high chance of ballistic transport. In reality however, the presence of sub-surface charge carriers in graphene supported by a dioxide substrate affect the transport of electrons severely, thereby reducing mobility and hindering ballistic transport. It is only by chemically etching the dioxide layer below graphene and current annealing it that the effect of these "charge puddles" can be removed. Low temperature transport measurements of "suspended graphene" have revealed mobility of 200 000 cm^2/Vs and mean-free path of the order of $2-3$ μm [26]. Near-ballistic transport has been observed in these samples, both at and away from CNP, for temperatures lower than 100K [27]. Unlike supported graphene the mobility of these samples depend considerably on carrier concentration and hence are unlikely to show ballistic behaviour for concentrations greater than 10^{13} cm^{-2}.

In the next section a unique way of fabricating useful devices by exploiting the geometrical dependence of conductance, in a ballistic transport regime, will be discussed. As will be seen a range of operation can be obtained from certain simple geometrical patterning of the active device.

2.3 Three terminal ballistic junctions

Over the last couple of decades several electronic waveguide structures have been proposed and analysed for being a functional nanoelectronic device to take advantage of a ballistic electron system. The Y-branched switch (YBS), has in particular, been considered for low-power, high-speed electronics, especially in its non-linear regime of operation. When the dimensions of the YBS are shrunken to a scale conducive to ballistic transport they can be considered as a three-terminal ballistic junction (TBJ). The following sections will analyse the principal-of-operation of such devices followed by practical results demonstrated so far and possible applications.

2.3.1 Principle of operation

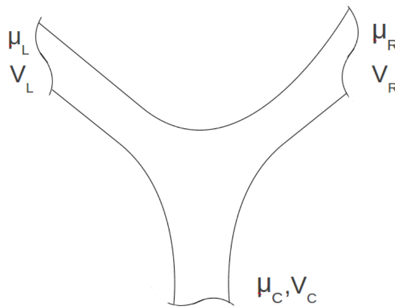

Figure 5: *Schematic representation of a TBJ with adiabatic boundaries*

A TBJ, or for that matter, YBS can be operated under many configuration; the one being discussed here would pertain to the case where voltages are supplied to the right and left branches and output is measured at the central branch. A simple schematic of such an arrangement is shown in Fig. 5. Here, μ_i and V_i represent the the electrochemical potential and voltage applied at the ith ($i = L, R$ or C) branch, respectively; they are related as $\mu_i = \mu_F - eV_i$, where μ_F is the chemical potential of the system at zero bias voltage. For nanoscale operation of multijunction mesoscopic system, where inelastic scattering is negligible, the transport properties are better described by the Landauer-Büttiker theory than the more common drift-diffusion theory. According to L-B formalism the current I_i flowing into the ith branch, at an energy E, is given by the relation [24]:

$$I_i(E) = \sum_{i \neq j} \frac{e}{h} f(E - \mu_i) T_{ji} - \sum_{i \neq j} \frac{e}{h} f(E - \mu_j) T_{ij}$$

where, $f(E)$ and T_{ij} are the Fermi-Dirac distribution and the transmissivity from the jth to the ith branch, respectively. For a vanishingly low applied voltage, the transmissivity can be considered to be constant for low temperature operation. In this so called linear regime the potential through the central branch would be a simple average of the potential of the left, and, the right branch. This is the intuitive conclusion from the more familiar drift-diffusion perspective too.

The same approach was extended for operation of TBJ under higher applied bias by Xu [7], with an important caveat - the energy dependence of transmissivity was explicitly taken into consideration. Under this model the current from the central branch is given by:

$$I_C = \frac{e}{h} \int \left\{ [T_{LC}(E) + T_{RC}(E)] f(E - \mu_c, T) - \sum_{i=L,R} T_{Ci}(E) f(E - \mu_i, T) \right\} dE, \quad (9)$$

Solving this equation with $I_C = 0$ gives the value of μ_C, from which the central branch voltage can be found out. For a junction where the left and right branches are symmetrical, it was shown that $T_{LC} = T_{RC} = (h/4e^2)G_C$, where G_C is the conductance of the central branch. Thus, for a symmetric, adiabatic ballistic junction, V_C is determined solely by G_C, and is independent of the structure of left and right branch, as well as included angle. When input voltage is supplied in a push-pull fashion, i.e., $V_L = -V_i$, and, $V_R = V_i$, V_C is derived from Eq. 9 as [7]:

$$\begin{aligned} V_C &= -\frac{1}{2}\alpha V_i^2 + \mathcal{O}(V_i^4), \\ \text{where} \quad \alpha &= -e \frac{\int G_C(E) \frac{\delta^2 f(E-\mu_F,T)}{\delta E^2} \, dE}{\int G_C(E) \frac{\delta f(E-\mu_F,T)}{\delta E} \, dE} \end{aligned} \quad (10)$$

Thus, for the discussed configuration, the output voltage V_C depends quadratically on input voltage V_i. Furthermore, for $\delta G_C/\delta \mu_C > 0$ (i.e., the transmissivity of the branch increases with potential), the so called non-linearity factor $\alpha > 0$ and V_C is always negative, being zero only when V_i is zero. This behaviour is displayed graphically in Fig. 6a. Results for an asymmetric TBJ where the right branch has a stronger lateral confinement is given in Fig. 6b. It can be seen that in addition to

the non-linear behaviour, the non linearity becomes weaker (i.e., $|\alpha|$ decreases) as the electro-chemical potential of the system is increased.

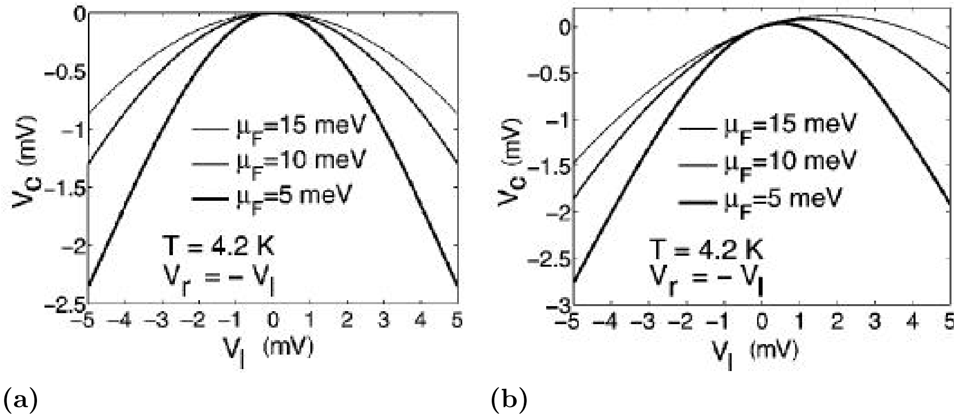

Figure 6: *Voltage output from central branch vs applied bias voltage for a.symmetric, and b.asymmetric TBJ [7]*

An alternate theory proposed to explain the non-linear behaviour of nanojunctions, albeit specific to the material in use, is the non-uniform distribution of electric field and charge carriers in the horizontal branch under application of push-pull voltage [28]. Under low bias the imbalance is caused due to a combination of space charge effects and the ballistic transport of electrons. For higher biases the inhomogeneity is due to the intervalley transfer mechanism in the semiconducting material. An important ramification of the Monte-Carlo simulations based on this mechanism is that V_C is linearly dependent on $-V_i$ (instead of $-V_i^2$) for higher bias voltages. As this semi-classical model explains non-linearity in the presence of scattering processes, it somehow relaxes the necessity of having coherent, ballistic transport [29].

In spite of some recent reviews (e.g. [30, 31]) the study of nanojunctions, ballistic or otherwise, in high-bias, high-temperature regime is in its infancy and needs further investigation.

2.3.2 Implementation

Most of the initial experiments on three terminal devices were done on high mobility heterostructure like GaAs/AlGaAs or GaInAs/InP with the junction size being smaller than, or comparable to, the mean free path of electron in room temperature. The devices included both Y-shaped and T-shaped structure, with additional side

or top gates to aid modulation of the electrochemical potential of the system. All structures showed the strong negative, non-linear behaviour as predicted in [7], at low as well as room temperatures (e.g. Fig. 7) [32, 33]. Further experiments revealed that at slightly higher input bias ($V_i > 300$ mV) the output becomes linear, as was pointed out in [28]. Interestingly, the non linear behaviour seen in ballistic junctions persisted in structures with dimension larger than the mean free path of electrons; ballistic behaviour in these large devices was explained by bias-induced enhancement of the mean free path [34]. Further studies demonstrated that, at low temperature, both large and small devices have identical non-linear behaviour (the threshold for transition to the high bias linear regime does decrease with device size). At higher temperature, however, the larger devices show considerable weakening of curvature with occasional null output for very small bias [35].

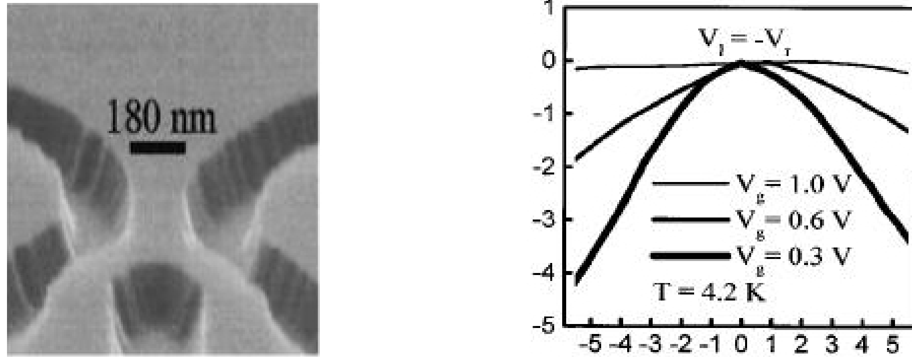

Figure 7: *A TBJ with 180nm waveguide and measurement results at 4K [32]*

Non-linear behaviour has also been demonstrated on TBJs fabricated from nanowires, nanotubes [36] and silicon [37]. Recently rectification effect was obtained from three terminal junction fabricated on supported single layer graphene [8]. The size of the junction (a STM image can be seen in Fig. 8a), was 200 nm; mean free path in the structure was estimated to be 70 nm. In spite of the diffusive nature of the device non-linear behaviour was obtained in a push-pull configuration, as is evident from Fig. 8b. The curvature is quite strong at 77K, degrading, but nevertheless remaining non-linear, at room temperature.

From the low temperature measurements in Fig. 8b it can be observed that, for $V_{bg} = +7V$, i.e., in the electron transport regime (the Dirac point was found out to be at $V_{bg} = +3V$) the output voltage remained negative; in the hole transport regime ($V_{bg} = -7V$), however, the output voltage was positive for all values of input voltage. This change of sign was explained in terms of the schematic presented in Fig. 9 -

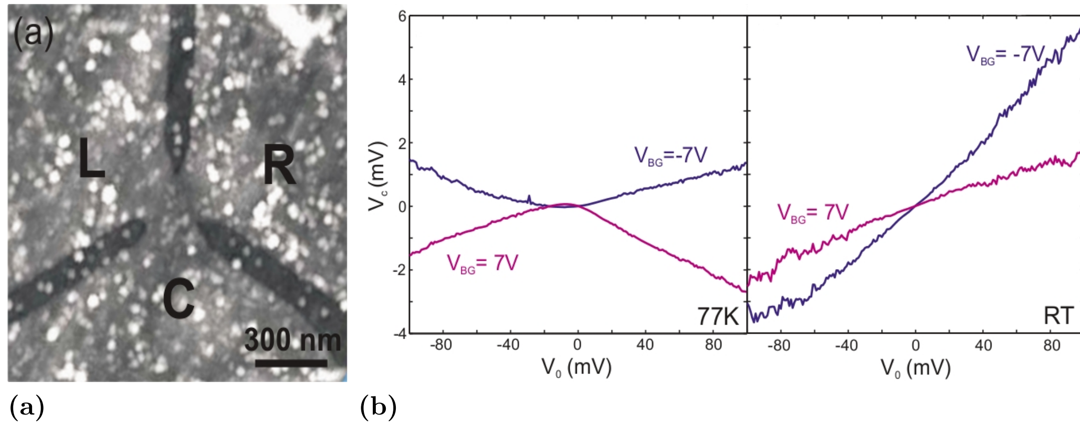

(a) **(b)**

Figure 8: *a. STM image of three terminal junction fabricated on graphene; b. Output voltage in a push-pull configuration at 77K and RT [8]*

it presents the difference of conductance G_{Ci} $(i = L, R)$ between two terminals of the struture, as a function of electrochemical potential μ. As can be seen, G_{Ci} increases with the potential in the electron transport regime, and vice-versa. Now, in order to maintain $I_C = 0$ in a push-pull confuguration, the potential of the central terminal would follow the potential of the terminal with higher conductance. In the electron transport regime the terminal with a negative applied voltage has higher conductance, and hence the output, too is negative. A similar argument could be put forth in the hole transport regime where the terminal with higher conductance has a positive voltage applied to it. An important corollary of this assumption, as was presented in the literature, was a progressive weakening of the output curvature as the system is tuned away from the Dirac point.

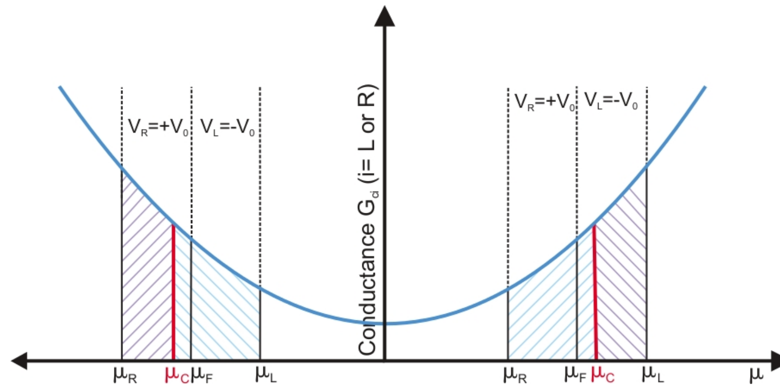

Figure 9: *Schematic explaining change of sign of output voltage due to back-gate voltage in a graphene TBJ[8]*

From the examples above it can be deduced that the predicted non-linear ouput from a three terminal nano-junction, operating in a push-pull configuration, is in no way limited to devices with ballistic transport. This is significant for graphene devices, as in Sec. 2.2 it was pointed out that only suspended graphene can exhibit true ballistic transport. The observation made in [8] confirms that non-linear operation can be extracted from graphene in the diffusive transport regime. As the device structure used in the literature was more akin to a nano-constriction, it would be useful to know the behaviour of a graphene device with a conventional Y-branch, or, T-branch structure. Before going into the details of fabricating such device on graphene some of the proposed application of TBJ devices would be presented next.

2.3.3 Applications

The basic push-pull configuration outlined in the above discussion can be used to make rectifiers, frequency multipliers and even logic gates. The rectification effect is obvious - when two out-phase ac voltage signals are applied to the left and right branches of a symmetric TBJ, the output voltage from the central branch is always negative. The quadratic output can be filtered out to obtain second and higher-order harmonics of the input, thereby allowing the use of TBJ as frequency multiplier. A circuit configuration made on a $Ga_{0.25}In_{0.75}As/InP$ based heterostructure that simultaneously exhibits the rectification and frequency multiplication effect of the TBJ is shown in Fig. 10 [38]. A TBJ can also be used as a logic gates when separate dc voltages are applied to the input branches [7]. With a little variation to the push-pull configuration, viz. by grounding or modulating the power source to one of the branches the TBJ can exhibit diode and transistor characteristics [39].

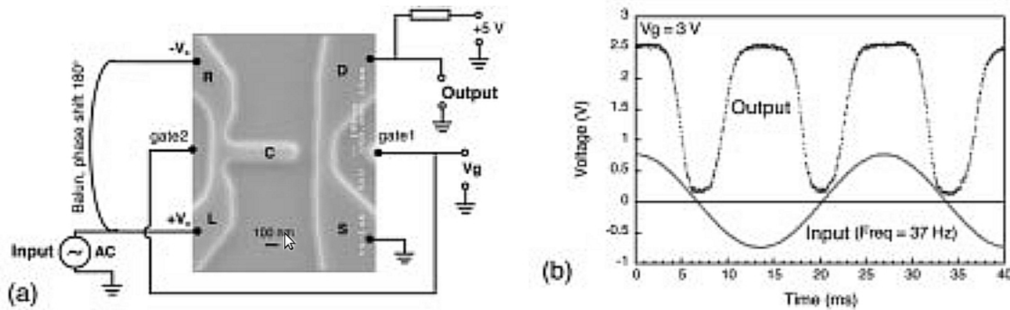

Figure 10: *Frequency multiplier using TBJ: a. SEM image of device with circuit schematic; b. Results [38]*

Three terminal ballistic junction have some unique advantages when compared

to conventional devices [40]. Lack of junction or gate capacitance, typically assosciated with semiconductor diode or MOS structures, means they have very low intrinsic capacitance. Thus, TBJ has an implicit advantage when it comes to high speed operations - of no less importance is the fact that they are compatible with HEMT devices. Rectfication through TBJ is not limited by any threshold, commonly seen in semiconducting rectifiers. Furthermore, the non-linear behaviour, at least in truly ballistic devices, persist for a long temperature range without any significant deterioration. These factors, combined with the characteristic low power requirement of nanoelectronic devices and apparent ease of fabrication, make it a strong contender for future use in high-speed, low-power electronics.

3 Experimental methods

With the theoretical background on the components that constitute the matter of this thesis being explained, it would be instructional to examine various avenues towards achieving the goal of fabricating three-terminal junctions on graphene. Issues that are likely to arise are, how graphene can be synthesised in a reliable and consistent way to give enough opportunity to fabricate meaningful structures on them. The question of identification and confirmation of whether the synthesised sample is indeed MLG is also important. Finally, a brief review of the methods required to fabricate nano-scale structures on a prepared sample is required to pick and choose the means most pertinent to achieve the end in question.

3.1 Synthesis of graphene

As has been outlined in Section 2.1 growth of 2-D crystals forbid certain basic principles of nature. However, in theory, the principles of artificially growing 2D crystal structures like graphene is rather simple, notwithstanding regular failures in achieving to do so in last century. It simply consists of growing a monolayer inside or on top of another crystal and then removing the bulk at sufficiently low temperatures such that thermal fluctuations are unable to mould them into 3D shapes.

One of the ways to achieve this is to mechanically split a strong layered material like graphite, where in-plane C-C Ω bonding are stronger than inter-layer π bonds, into individual atomic planes, the so called *micromechanical cleavage* method. Earliest attempts to isolate graphene tried were focused on chemical exfoliation of bulk graphite using large-molecule intercalating species; however results were not satisfactory [41]. Truly 2D crystals were first obtained by using micromechanical cleavage in 2004 [2]. This “scotch-tape” method of extracting graphene is a rather simple and inexpensive process to produce crystals of high structural and electronic quality. It consists of putting graphite flakes on the adhesive side of a scotch tape and repeatedly peeling them off using same/different tape to obtain a layer of fine graphitic granules. These are then transferred to a suitable substrate, most commonly SiO_2, by pressing it firmly onto the tape - some of the granules thus transferred turn out to be graphene flakes, albeit of varying thickness, width and shape. These flakes are attached to the substrate, most likely due to van der Waals and/or capillary forces. A step-by-step depiction of the method underlined above is shown in Fig. 11. The process outlined above can be automated, to a degree, by

means of ultrasonic cleavage [42] to obtain a stable suspensions of sub-micrometre graphene crystallites. In this work, however, the simple "scotch-tape" method was used to produce graphene.

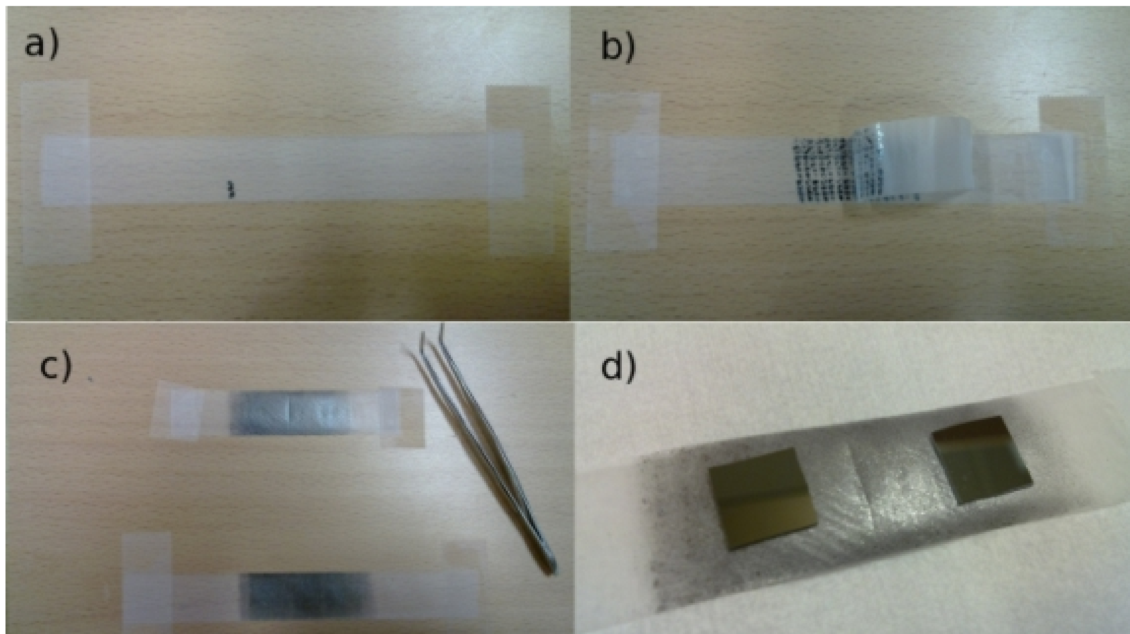

Figure 11: *Micromechanical cleavage of graphene by scotch-tape method*

As a passing note, it is worth mentioning that though micromechanical cleavage remains the technique of choice for making proof-of-concept devices, the tedious nature of the process renders it unsuitable for industrial scale production. The answer lies in various methods to produce graphene *epitaxially*. The earliest attempts targeted growing graphene on the Si-terminated (0001) face of single-crystal 6H-SiC by the thermal desorption of Si [43]. Chemical routes of producing graphene by reduction of graphene oxide have also been tried [44]. The focus nowadays is on deposition of graphene on sheets of transition metal (like copper, cobalt or nickel) using decomposition of hydrocarbons. Good results have been obtained from chemical vapour deposition employing decomposition of gaseous sources like CH_4, C_2H_4, C_2H_2 and benzene [45], as well as solid carbon sources like PMMA and sucrose [46]. With optimisation of substrate material, growth, and transfer procedures this method seems to show real promise of producing large-scale, high-quality graphene [47, 48].

3.2 Characterisation of graphene

Characterisation of graphene is a broad field that encompasses investigation of the number of layers in a given sample as well as identifying surface states, ripples, defects and impurities on it. Owing to the unique two-dimensional nature of graphene, each of these factors have profound effect upon the ultimate electronic nature of the sample. A variety of techniques have been used to study the property of graphene produced by different method [49], as well as its behaviour under varying ambient. Of these, Transmission Electron Microscopy (TEM), Atomic Force Microscopy (AFM) and Raman Spectroscopy are the ones used most widely and effectively. In this work the last two methods have been used to identify number of layers and impurities on isolated graphene flakes.

Using mechanically exfoliated graphene incurs the additional step of locating the flakes on a substrate, which is typically populated with thicker graphitic flakes, adhesive glue and other impurities. This is a tedious process and none of the sophisticated visualisation techniques mentioned above, is capable of concurrently identifying and characterising graphene, primarily due to their low throughput. Currently the only way of identifying cleaved graphene is to carefully scan the surface of the substrate with an optical microscope.

3.2.1 Optical microscopy

Although graphene is nominally transparent to visible light, even a single layer of graphene, when put on a suitable substrate, adds up enough difference in the optical path to be identified by naked eye. The origin of this optical contrast between MLG and underlying SiO_2 substrate can be explained with the aid of Fresnel's Theory of double refraction [50]. It has been found out to be a function of the thickness of oxide layer as well as the spectrum of source light, as can be seen from Fig. 12.

With the aid of specialised filters, graphene can be visualised on top of SiO_2 of practically any thickness, except for ≈ 150 nm and below 30 nm. Without any filter, thickness of 90 nm and 280 nm are most suitable, with the lower thickness providing a better choice. In practise, a thickness of $250 - 300$ nm is used. It must be noted that even a 10% change of thickness beyond this limit reduces visibility sufficiently to render graphene, especially MLG, invisible. This can be seen in Fig. 13c, where graphene deposited on a 200 nm thick SiO_2 is practically invisible as compared to Fig. 13a, where a 300 nm thick dioxide layer has been employed and a clear

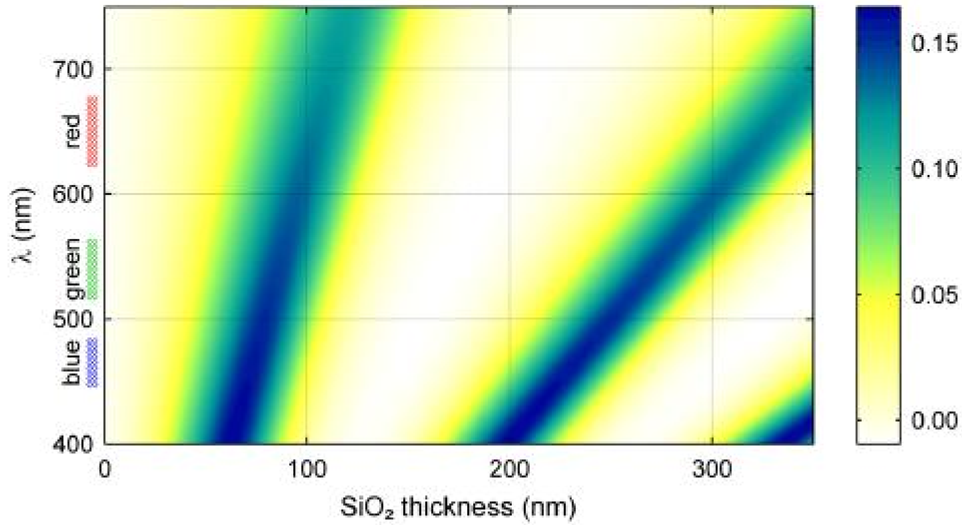

Figure 12: *Contrast of MLG as a function of wavelength and thickness of SiO_2 substrate [50]*

contrast between the different graphene layers exists. The increase in contrast due to employment of filters can be seen in Fig. 13b where green ($\lambda = 560$ nm), instead of white light has been used.

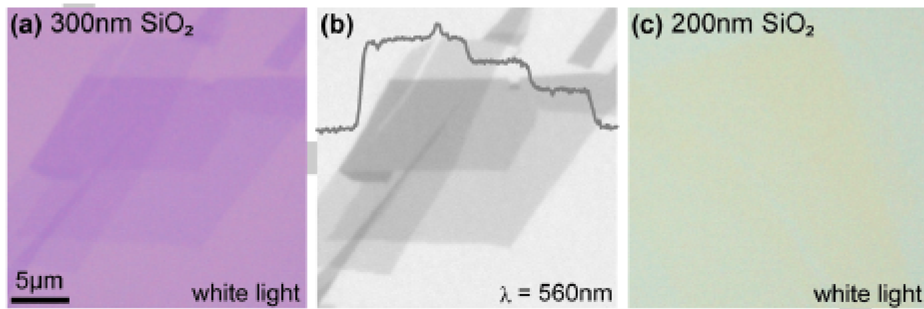

Figure 13: *Graphene crystals on 300 nm silicon dioxide layer imaged with a. white, and, b. green light. c. Another graphene sample on 200 nm thick dioxide layer [50]*

Optical microscopy, in isolation, cannot be used to quantitatively separate MLG from BLG or FLG, although with sufficient experience, a user can make an intelligent guess about the thickness of graphene crystal. For better result more sophisticated methods like AFM or Raman spectroscopy must be used.

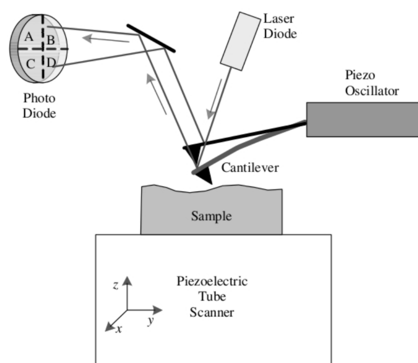

Figure 14: *Schematic of Atomic Force Microscope*

3.2.2 Atomic force microscopy

Atomic Force Microscopy, invented in 1986 by Binnig and Quate [51], has become a method of choice to study surface topography. A schematic of a typical AFM arrangement is given in Fig. 14. When the tip is brought into proximity of a sample surface, forces between the tip and the sample (primarily, but not limited to van der Waals forces) lead to a deflection of the cantilever according to Hooke's law. The deflection is detected from the laser beam reflected from the cantilever into a two-segment or four-segment position sensitive photo-diode. Holding this signal constant, by varying the sample height through a feedback arrangement, gives the sample height variation, as the tip is scanned across the surface using piezoelectric components. Topography of a sample can be extracted with an AFM in contact, non-contact oscillating, or, tapping mode. Of these, the first one is prone to surface damage, and, the second one suffers from low sensitivity. Hence, AFM is operated mostly in intermittent-contact oscillating (or, tapping) mode. It is achieved by allowing, during scanning, the vertically oscillating tip to alternately contact the surface and lift off at a frequency of 50 to 500 KHz. The amplitude of oscillation is larger than 100 nm, and amplitude detection is used. It allows for high vertical resolution with negligible surface damage. AFM is a versatile technique that can be used for both conducting and insulating surfaces under a variety of ambient conditions.

AFM is especially useful to differentiate MLG and BLG from FLG. Considering that the inter-layer thickness of graphene is $\approx$ 3.35 Å, it can be said that a modern AFM with its high resolution would be able to differentiate up to a single layer. However, there exists a certain chemical contrast between the substrate and

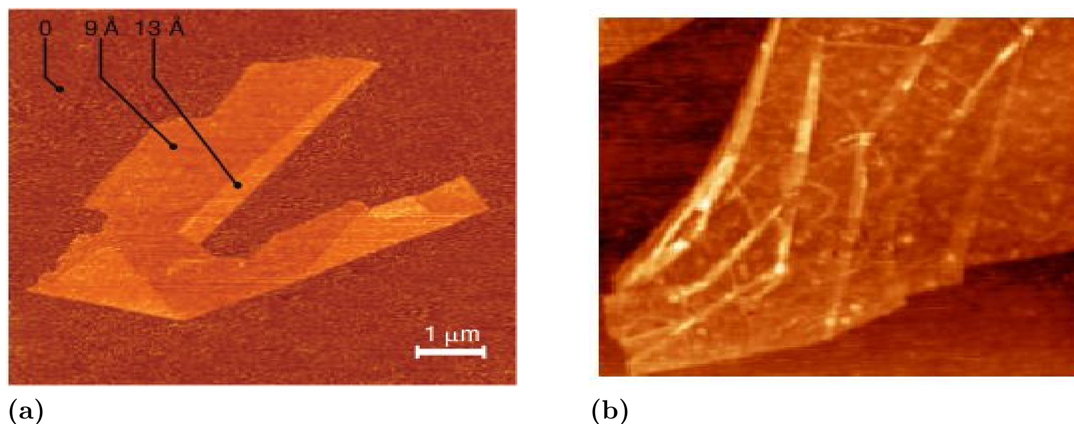

(a) (b)

Figure 15: *a.AFM image image of graphene showing areas of varying thickness, an indication of number of layers ; b.Another image showing folds and crumples that occur between the transition of layers in graphene [2]*

graphene, which causes the AFM tip to be more strongly attracted to the SiO_2 substrate. There also exists a certain "dead layer" of absorbed water between the crystal and substrate [52]. This results in an apparent chemical thickness of $0.5 - 1$ nm for MLG, when observed in AFM, rendering differentiation between MLG and BLG slightly difficult. For FLG the apparent thickness is more than 1 nm. Even so, AFM is a very useful tool to observe the surface topography of graphene crystals deposited with the scotch-tape method, as can be seen in Fig. 15a . It is the only conceivable tool to study the folds and crumples in graphene (seen in Fig. 15b) that apparently renders it stable against possible decomposition into smaller islands of greater thickness.

3.2.3 Raman spectroscopy

Raman spectroscopy, is in its simplest terms, a light scattering technique that can be used for chemical identification, the characterisation of molecular structures, the effects of bonding, the environment and stress on a sample. As will be seen here it can be used very efficiently to identify and isolate layers of graphene quantitatively with high accuracy.

Raman spectroscopy is based on a phenomenon called Raman scattering, discovered by C.V. Raman in 1928. When monochromatic radiation is incident upon a sample then the back-scattered light consist mostly of the photons with same energy and wavelength as the incident photons (Rayleigh scattering). Yet a

very small part of the photons (≈ 1 in 10^7) are backscattered inelastically with a different wavelength than that of the incident photon. The process leading to this inelastic scattering is termed the Raman effect. Raman shifted photons of light can be either of higher (anti-Stokes scattering) or lower energy (Stokes scattering), with the former being weaker of the two processes. Numerically, the energy difference between the initial and final vibrational levels, or Raman shift in wave numbers (cm^{-1}), is calculated as the difference between the inverse of the wavelengths (in cm) of the incident and Raman scattered photons [53].

Modern day Raman spectroscopes consist of lasers, optics, detector systems and a sample stage as illustrated in Fig. 16. The desired area of the sample is scanned with coherent light from the laser, which is guided through a delivery optics (microscope) to the sample surface. The scattered light is then collected and sent through a monochromator to a photodetector. The function of the monochromator is to remove Rayleigh scattered photons. Finally, to get the Raman spectrum, the intensity of the scattered light is plotted against the Raman shift (energy difference).

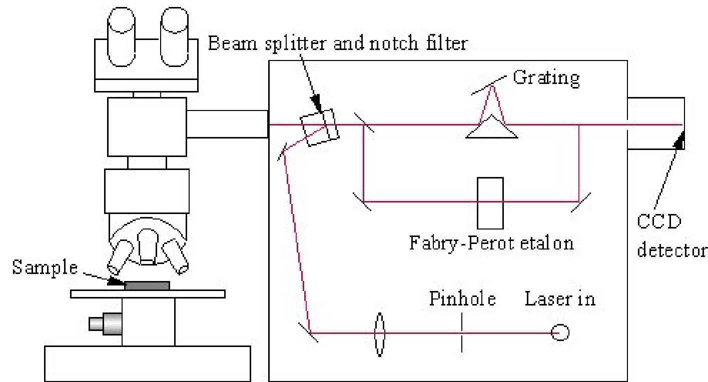

Figure 16: *Schematic of a modern day Raman spectrometer*

The Raman spectrum of graphite has four prominent peaks [54]. The peak at around 1580 cm^{-1}, known as the G line, is caused by the doubly degenerated zone centre E_{2g} mode close to the Dirac point. The D line around 1350 cm^{-1} is seen only in disordered graphite and is caused by zone-boundary phonon. The associated overtone $2D$ (also known as G') at around 2700 cm^{-1} however is observed even in pristine samples. Finally, a weak peak is observed at the overtone of the G line, the $2G$ line, at around 3248 cm^{-1}.

For the purpose of identifying the number of layers the G peak and $2D$ band are of paramount importance [55]. As can be seen in Fig. 17a and Fig. 17b there

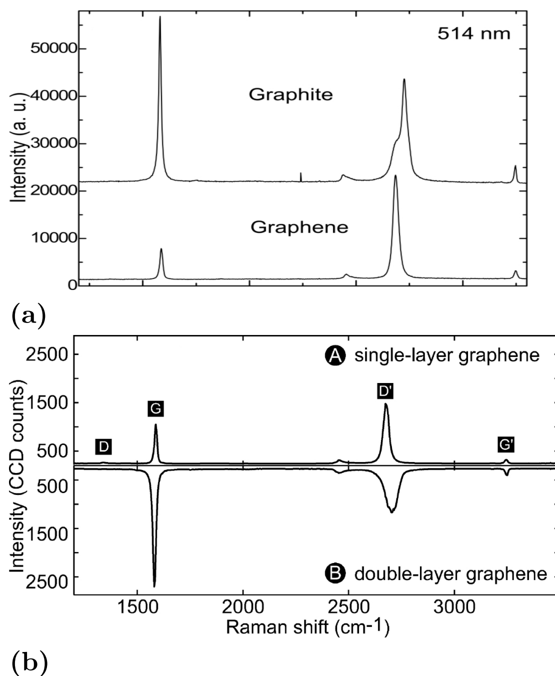

Figure 17: *Comparison of Raman spectra for a.bulk graphite and graphene [55], and, b.for MLG and BLG [54]*

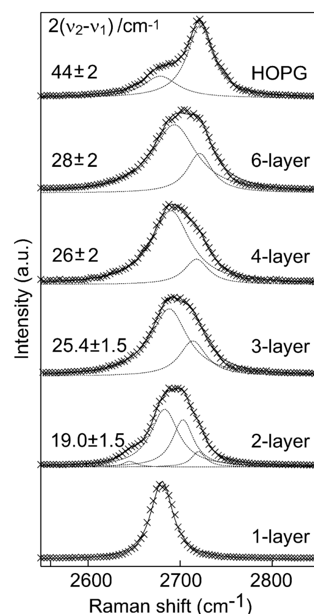

Figure 18: *Progression of 2D band of graphene layers [54]*

is a significant change in shape and intensity of $2D$ peak in MLG when compared to BLG or bulk graphite. MLG is characterised by a single, sharp $2D$ peak, greater in intensity than the G peak. In BLG and bulk graphite, the $2D$ peak broadens to form a band and its intensity is increasingly lesser than the corresponding G peak. In fact, the width of $2D$ band continues to increases with the addition of each extra layer; beyond 5 or more layers the width becomes comparable to that of graphite. For BLG, the $2D$ band can be fitted into 4 components, whereas that for FLG and graphite can be fitted into 2 components, as is shown in Fig. 18 [56]. The intensity of the G-peak intensity depends on the number of layers too - as the number of layer increases so does the intensity of the peak. An increase in number of layers is also marked by a marked downshift in the position of G peak.

3.3 Fabrication on graphene

Fabrication of any sort of devices on graphene present some peculiar challenges. As the aim is to get nano-scaled device from samples strewn randomly on a substrate, traditional photolithographic techniques are out of the question. Hence,

nanolithographic techniques like Electron Beam Lithography (EBL) and Focused Ion Beam Lithography (FIB) must be investigated to come up with a suitable solution for making, at the least, proof-of-concept devices. Care must also be taken to avoid aggressive lithographic and etching techniques that might damage the single layer thick crystal. Another contentious issue is that of fabricating metal contacts that can be employed to make useful electrical characterisation of the obtained device.

3.3.1 Nanolithography

Electron beam lithography is a specialised, and nowadays, the dominant technique for creating nanoscaled patterns. Based on Scanning Electron Microscope (SEM), the technique in brief, consists of scanning a beam of electrons across a surface covered with a resist film sensitive to those electrons, thus depositing energy in the desired pattern in the resist film. The main advantage of this technology is its capability of very high resolution and its flexibility. However, it is a slow process with expensive and complicated mechanisms.

A block diagram of a typical electron beam lithography tool is shown in Fig. 19 [57]. The electron source in most modern day EBL's are Schottky (thermal field emission) guns as they have a high ampere per steradian output with a low energy spread, although LaB_6 sources are sometimes preferred for their stability. The emitted electrons are accelerated under high voltage and made to pass through a series of magnetic lenses to shape and focus the beam through an evacuated column. The final pattern size and accuracy largely depends upon the number and energy of electrons hitting per unit surface area (commonly known as dose), the speed with which the beam traverses over the surface, the accelerating voltage and the aperture size used to shape the electron beam. A great deal of precision automation is embedded into the system to enable control over these variables. High accelerating voltage with low beam current and small step size with average beam speed give best results, provided of course that focusing and astigmatic corrections are proper. A Zeiss Supra 40 Scanning Electron Microscope with Raith Quantum pattern generator was used extensively during the course of this thesis work, both to obtain high resolution images as well as for nanolithography. It employs a Schottky field emitter, with an acceleration voltage range of 100 V to 30 kV and a beam current range of 1 pA to 10 nA. It offers lateral resolution of up to 0.8 nm (at 30 kV) in the SEM mode - small enough for the purpose of this work.

Electron beam resist are generally polymers dissolved in a liquid solvent; electron

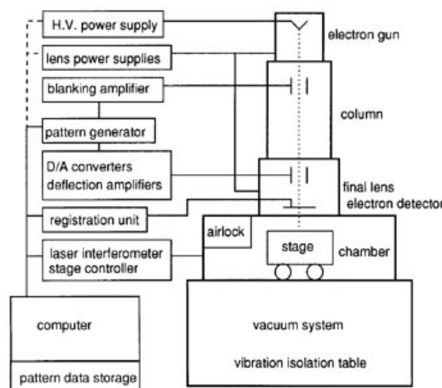

Figure 19: *Block diagram of an Electron Beam Lithography tool*

exposure modifies the resist, leaving it either more soluble (positive) or less soluble (negative) in a developer. The type of resist and its underlying chemistry determines film thickness, exposure dose, development time, etc. Positive resist like Polymethyl methacrylate (PMMA) are preferred because of the simplicity and predictability of their chemistry [58]. The sensitivity of PMMA scales roughly with electron acceleration voltage. It has an intrinsic resolution of less than 10 nm, although, electron-solid interactions introduce a bias of 20 - 150 nm. It is normally dissolved in casting solvent such as chlorobenzene or anisole and developed using Methyl isobutyl ketone (MIBK). MIBK, in isolation, is a strong developer and might remove some of the unexposed resist. Hence it is usually diluted by mixing it with a weaker developer such as Isopropyl alcohol (IPA). The level of dilution of PMMA and MIBK directly influence the dosage and exposure time. PMMA has poor resistance to plasma etching; hence, frequently it is used with an addition layer of Methyl methacrylate (MMA). This is also useful for lift-off processes because of the favourable undercut and reduced stiction to surface.

Focused Ion Beam lithography is a commonly used technique for site-specific analysis, deposition, and ablation of materials. An FIB setup is conceptually similar to a SEM, but uses a focused beam of ions instead of electrons. For production of an ion beam the common medium of choice is liquid-metal ion sources (LMIS), especially gallium ion sources. FIB is commonly used in conjunction with other gases to either etch surfaces or deposit material on them. One important advantage of FIB based lithography over EBL is that it does not require use of any photoresist, thereby vastly simplifying patterning process. However, the ion beam is inherently destructive and cannot be used with sensitive samples; furthermore it tends to get

trapped in material underneath, thereby introducing impurity.

3.3.2 Metalisation

To utilise the structures fabricated on graphene, metal contacts must be drawn. This can again prove to be a contentious issue - the basic physics behind the contact junction must be taken into consideration while choosing the metal contacts on graphene. The aim, of course remains to find a metal that would enable formation of an ohmic junction - such conditions can be obtained only when the work function of graphene and contact metal is evenly matched and ionisation energy of the resultant system is zero. Even under ohmic conditions, contact resistivity should be sufficiently low to avoid charge accumulation and heat dissipation. Certain metals can be straight away ignored as they alter the electronic structure of graphene. Ohmic contacts require that the work function of metal must be closely matched to that of graphene (4.5 eV). The best contenders are titanium Ti (3.9 eV), chromium Cr (4.5 eV), molybdenum Mo (4.6 eV) and palladium Pd (5.1 eV). Normally, metals are deposited in pair with the underlying metal forming the metal-graphene junction and the top buffer metal providing for improved contact to external devices. The most commonly used metal pairs are Pd/Al, Cr/Au, Mo/Ti and Ti/Au. Among these, the Cr/Au and Ti/Au combination display better values of contact resistance and sheet resistivity [59], with the second combination being chosen in this work due to its robustness. Contact resistance also depends on the thickness of deposited metal; for Ti/Au good results are obtained for a deposited thickness of $\sim$ 5 nm and $\sim$ 35 nm respectively.

Deposition of metal is most often done by one of the many physical vapour deposition processes [60]. The principle behind this is rather straight forward - heat the target material to eject energised particles from it and enable transport under high vacuum to the substrate. Reactive agents can be emitted from the target material using various means - by resistive heating (thermal evaporation), electron beam heating (e-beam evaporation), equilibrium source heating (molecular beam epitaxy), ion bombardment (sputtering) or laser bombardment (ablation). Out of these e-beam evaporation (Fig. 20) is best suited for metal deposition on graphene as it does not expose the fragile crystal to high energy particles, like in sputtering or ablation, or, high temperatures, like in thermal evaporation or MBE. The disadvantage is insufficient control over deposition rate and yield - this however can be overlooked as it does not cause any significant change to the final structure.

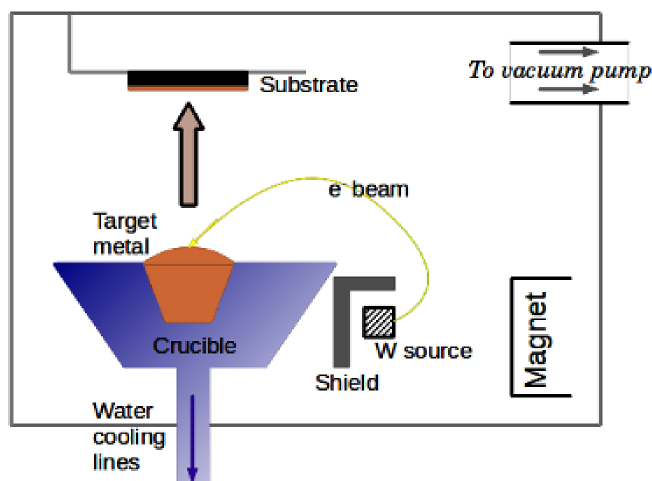

Figure 20: *Schematic for electron beam evaporation technique for metal deposition*

Even after choosing and depositing suitable metal for contact pads, the problem remains in how it can be patterned on graphene. Two common methods of metalisation exist in the semiconductor industry - direct deposition and deposition by “lift-off” technique [60]. In the first method metal is deposited on the surface and then etched away to get the required structure. In the second method, lithography with a negative pattern is first performed on the surface before depositing metal on it. Thus except for the developed part where metal is in direct contact with underlying surface, metal is deposited on resist. If the resist is removed after this step, only metal on patterned part remains. This is shown in Fig. 21. This technique has got the advantage of guarding underlying surface from harsh conditions and aggressive chemicals required for deposition and etching. Additionally, it allows for profile tailoring of deposited metal film. Hence the lift-off technique was adopted for patterning.

3.3.3 Etching

Etching of mono layer graphene is relatively straight forward. Chemically assisted etching, however, must be avoided - due to its surface absorption capability, graphene may easily trap reactive ions in its lattice. Though simple plasma etching is enough to etch away MLG, it results in jig jag edges. This can be problematic for nano-ribbons and alternate etching mechanisms employing thermally activated metal nanoparticles [61], etc. have been proposed. For structures approaching 100 nm,

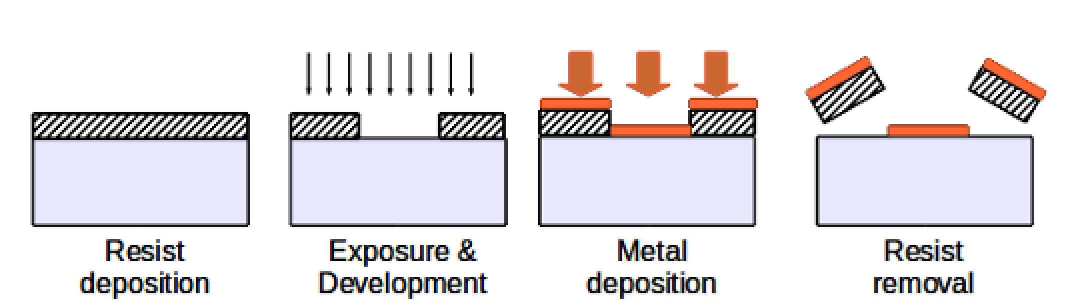

Figure 21: *Lift-off technique of metalisation*

however, uncontrolled edge termination is not a big handicap. Currently, oxygen plasma etching is the most widely used method [62]. Oxygen assisted etching in graphene proceeds by formation and merging of nano-sized "etch-pits" [63] and is a slightly volatile process. Hence, it is mixed with inert gases like argon to prevent damage to resist and adjoining graphene. The etch rate depends strongly on the partial pressure of component gases and an optimum combination is important to prevent inadvertent destruction of the film.

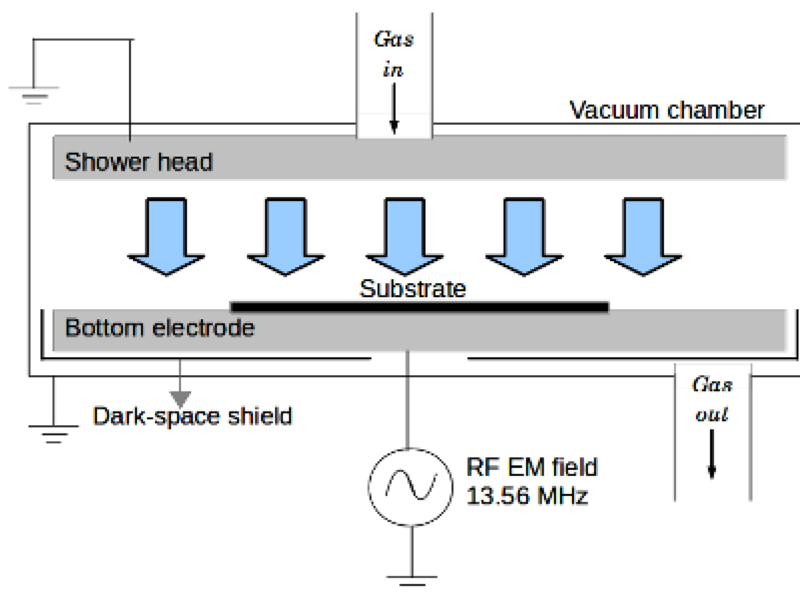

Figure 22: *Schematic of a parallel plate reactive ion etching chamber*

The dominant method of plasma etching is the parallel plate Reactive Ion Etching (RIE) technique [60], a schematic of which is shown in Fig.22. Etchant gases are introduced through the top electrode, which is kept grounded. Plasma is generated by applying a strong electromagnetic field, typically set to a frequency of 13.56 MHz,

to the bottom electrode. The wafers, being electrically isolated from the system, develop a large negative voltage. As a result the positively charged ions from the plasma collide with the sample at high velocity. Etching of the surface is carried out by ion-induced desorption, ion-induced damage and ion-activated chemical reactions.

Plasma ion etching typically leaves a lot of burnt carbon contamination, even in areas protected by the resist. In addition to this, the fabrication processes might result in polymer residues on the graphene film. Hence, a final annealing process, in ultra-high vacuum, or, in forming gases, is necessary to drive away impurities and reduce possible crystal damage. However, exposure to ambient after the annealing affects the doping density of graphene, sometimes irreversibly [64]. The medium and time of annealing decides the degree of doping and are factors that must be taken into consideration. Recent studies [65] have pointed out that thermal annealing might actually cause further contamination of graphene due to binding of foreign material from residual glue. However, in view of the widespread use of this technique as damage-reducing final step, it would be unwise to drop it summarily.

4 Fabrication techniques and results

The last section gave a broad, if not exhaustive, investigation of various approaches that can be employed to fabricate three terminal junctions from graphene. This section will present the actual methods used to synthesise, characterise and fabricate graphene, along with the obtained results.

4.1 Sample preparation

The first step in preparing graphene samples is of course developing a suitable substrate. To this end SiO_2 was thermally grown on a n-type Si(100) wafer with a resistivity of $10 - 15$ Ωcm. During the course of this work wafers with dioxide thickness of 245 nm and 305 nm were used. As can be seen from Fig. 23a and Fig. 23b these values of substrate thickness give sufficient contrast for graphene flakes to be visible. Thereafter, 100 nm deep cross-marks were patterned on the substrate using photolithography and BHF etching to obtain a $1\ mm \times 1\ mm$ grid-like structure across the surface. This was done for ease of locating deposited graphene flake at later stages of processing. Using a dicing saw the wafer was then sawed to $1\ cm \times 1\ cm$ square pieces. To get rid of residual photoresist and particle contamination, the chips were then subjected to ultrasonic agitation in acetone and IPA for 10 minutes each, followed by rinsing in deionised water (DIW) and nitrogen blow drying.

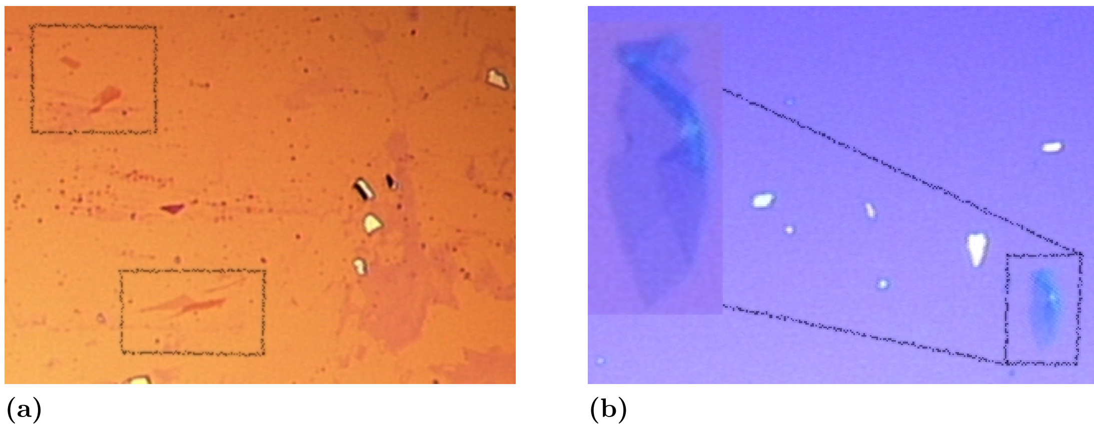

(a) (b)

Figure 23: *Micromechanically exfoliated graphene on a.245 nm (unclean), and, b.305 nm (inset shows rolled up MLG due to prolonged ultrasonication) thick dioxide layer*

High quality graphite flakes supplied by NGS Naturgraphit GmbH were used

as a starting material to obtain graphene. The "scotch-tape" method outlined in Sec. 3.1, and utilised in this thesis, typically leaves the surface strewn with graphitic granules and residual adhesive glue from tape (Fig. 23a). Therefore, ultrasonic agitation in acetone for 2 minutes, followed by rinsing in IPA and DIW was used to clean the substrate. Though this process did not remove the contamination fully, it was found out that the ultrasonication process tends to bend and roll graphene flake (inset Fig. 23b). Agitation for longer time left the flakes too disfigured for further use; shorter times left the surface too dirty for subsequent processing. After the cleaning process, bright-field optical microscopy under white light was used to isolate graphene (MLG, BLG and FLG) from thicker graphite flakes.

4.2 Sample characterisation

Characterisation of graphene, within the scope of this thesis, was limited to identification of number of layers in graphene flake that had been identified using optical microscope. To this end, the flakes were scanned with a NT-MDT Ntegra Aura AFM in tapping mode, at room temperature. A NSG-01 n-Si probe, with a 125×30 μm cantilever and an uncoated tip with the radius of curvature $6 - 10$ nm was used. Under the scanning condition and configuration a vertical resolution of 1 nm is supposed to be achievable. However, the provided setup was not optimum for unambiguous layer detection. As an example, Fig. 24 shows the AFM image of two graphene flakes; the variation in height, $4 - 6$ nm for both, does not confirm any appreciable difference between them. But even with optical microscopy, ample difference in contrast were obtained between these flakes to safely assume that they were not constituted of the same number of layers.

Consequently confocal Raman microscope alpha300R manufactured by WiTEC Gmbh was used to extract Raman signatures of prepared graphene sample. Measurements were obtained at room temperature with a 532 nm laser excitation on a back-illuminated spectroscopic charge-coupled device cooled down to -60°C. For spectrometry a single grating of 600 g/mm with a spectral unit parameter equal to 2050 cm^{-1} was used. To prevent surface damage as far as possible, low laser power, as well as, low signal acquisition times were used.

The results obtained thereof have been shown in Fig. 25; the spectra have been offset in y-direction for better clarity. They clearly show the increase in intensity and downshift of the G peak at ≈ 1580 cm^{-1} with the increase in number of layers. Position and intensity of the G peak was found out to be mildly dependent on

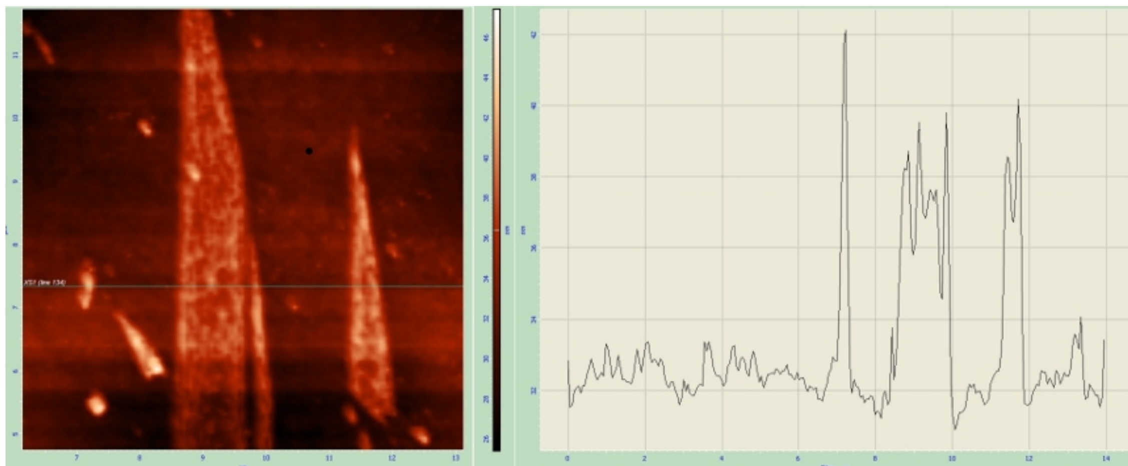

Figure 24: *Obtained AFM image of graphene flakes with the height variation across a horizontal cross section displayed on the right*

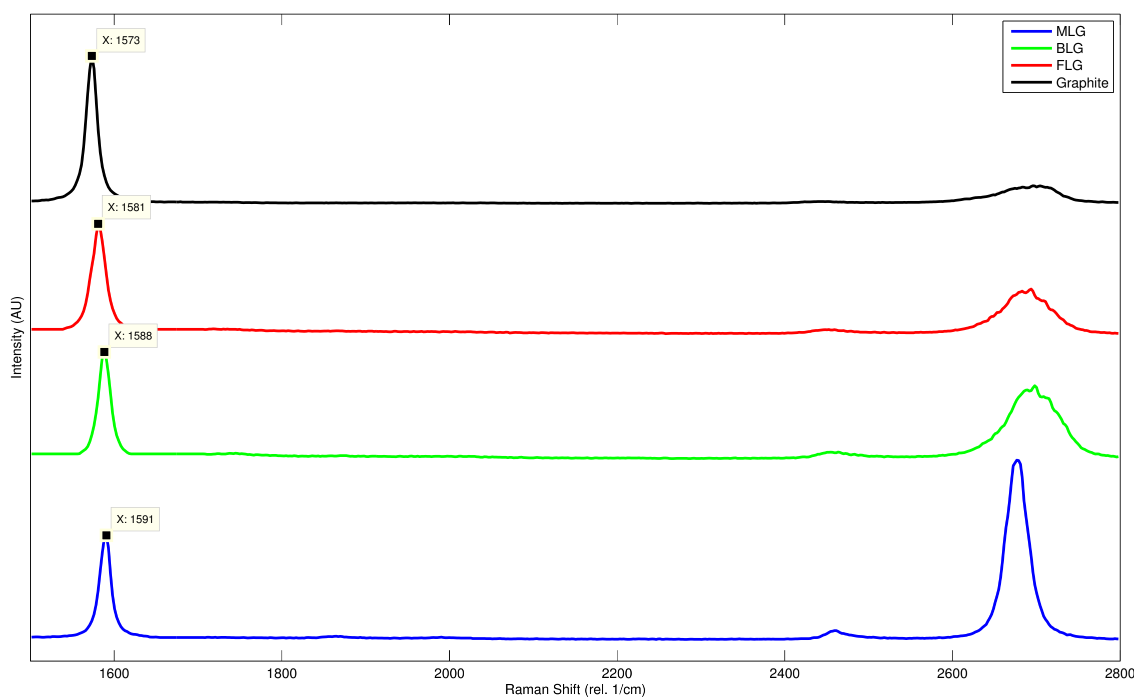

Figure 25: *Obtained Raman signature of different graphene flakes with varying number of layers*

applied laser intensity and integration time. Shape of the $2D$ peak, however did not suffer from such conditional anomalies. Identification of MLG, with its characteristic sharp and intense $2D$ peak, thus becomes straightforward. Identification of BLG from FLG required additional processing - spectrum deconvolution of the $2D$ band

was used to obtain Lorentzian peaks that fit the obtained data. An example has been given in Fig. 26. The measured data (blue dots) was fitted to 4 peaks (green line) centred at 2653, 2677, 2695 and 2712 cm^{-1}, with the final fit (red line) giving an error of 2.8%. This is a clear indication of the presence of BLG, as explained by the double-resonant model of graphene in Sec. 3.2.3.

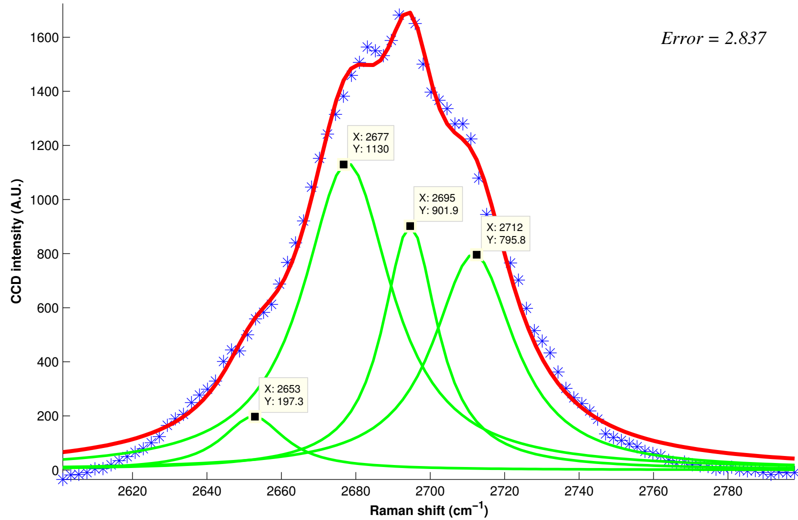

Figure 26: *Spectral deconvolution of 2D band of the Raman signature of a graphene flake*

4.3 Fabrication on sample

A number of geometries can be used to realise a three-terminal junction on graphene. It can realised as a nano-constriction between three wider regions of graphene, or, as a traditional T-shaped or Y-shaped device. Even among the latter class, the dimension of each branch and the angle between them can be varied. For the purpose of this work, the representative geometry was chosen to be a Y-shaped structure with the length and width of each branch being 1200 nm and 200 nm, respectively. The angle between the left and right branch was kept at 90°. Each branch terminated in a wider region of graphene, from which a thin metallic contact line was drawn to a 200 $\mu m \times 200$ μm metallic pad. A schematic of this structure is given in Fig. 27.

Both MLG and BLG flakes were used in this work to fabricate three-terminal junctions upon. The cross-marks etched on the substrate were found out to be too far-apart to be used for identification of flakes during nanolithographic processes.

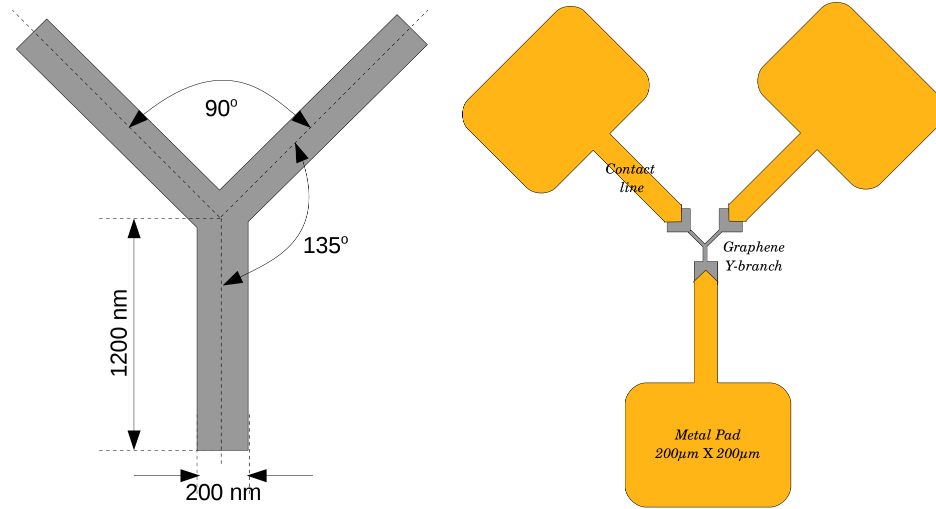

Figure 27: *Representative diagram of Y-branch fabricated on graphene*

Hence, the first step was to fabricate additional cross-mark at the corners of a 400 $\mu m \times 400$ μm square centred at the flake of interest. To this end, direct deposition of 80 nm high platinum cross-marks with FIB was attempted. A Helios Nanolab 600 Dual focused beam system, manufactured by FEI company was used. The process, however, was found out to be highly detrimental towards quality of graphene. It also left the surface strewn with organic contamination and poly-carbon dust - the contaminants are clearly visible in the AFM image of a BLG flake subjected to FIB deposition, in Fig. 28. For this reason, lift-off metalisation was performed to deposit 50 nm high gold cross-marks; the intricacies of the method would be given shortly.

The final structure could be obtained using one of two ways - deposit the metal lines required for metalisation, and then etch the graphene flake to desired shape, or, use the exact opposite order. Of these, the first alternative was utilised to obtain better control over final structure. The metal lines and pads were deposited using the lift-off technique. To this end, the chip was first rinsed in IPA-DIW solution and heated on a hot-plate at 90°C for two minutes. This step was included to remove any particle contamination, and, to drive away moisture from the substrate to ensure better adhesion of e-beam resist in the following spin-coating stage. Two layers were deposited - first, a solution of 6% MMA in ethyl lactate, and then a solution of 2% 950 K molecular weight PMMA in anisole. About 2 ml of MMA was dispensed on the substrate, which was then spun at 6000 rpm for 45 seconds.

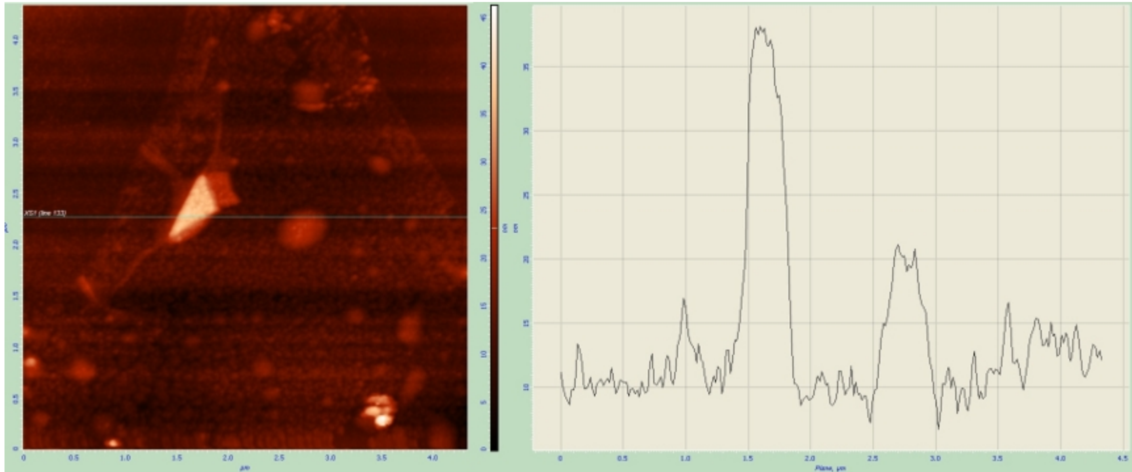

Figure 28: *AFM image of contaminations on a graphene flake after FIB-assisted Pt deposition*

The substrate was then baked on a hot-plate at 170°C for 150 seconds, primarily to evaporate the solvent and harden the resist. Thereafter, the same cycle was repeated for PMMA. According to the specifications given by Microchem Co., suppliers of the resist polymer, these spinning parameters should result in a MMA layer thickness of 400 nm and a PMMA layer thickness of 70 nm. Electron-beam lithography, with a beam acceleration voltage of 20 kV and dose of 225 $\mu C/cm^2$, was then performed to pattern the resist. The resist was then developed by immersing the chip in a solution of MIBK in IPA (in a ratio of 1:3; the ratio typically gives a very high resolution at the cost of low throughput and sensitivity) for 25 seconds at room temperature. To stop the development process, the chip was immediately immersed in IPA for about 10 seconds, and blow dried. The resulting pattern was checked under microscope and subject to longer development times, if required. After the final development, to remove any residual developer, the substrate was subject to a post-bake stage of 90°C for 60 seconds on a hot-plate.

Subsequently, e-beam evaporation technique was used to deposit 5 nm of titanium and 35 nm of gold on the resist. An Instrumentti Mattila 9912 Electron-beam evaporator, equipped with a 10 kV electron gun and a cryopump for deposition at $\approx 10^{-8}$ mbar, was used for this purpose. To wash away the resist, the substrate was kept in acetone heated to 70°C for 20-25 minutes. This process helped to seep the acetone underneath the unexposed resist; after this removing the resist, along with the metal layer above it, simply required ultrasonic agitation for few seconds. The substrate was thereafter promptly rinsed in IPA and DIW followed by nitrogen

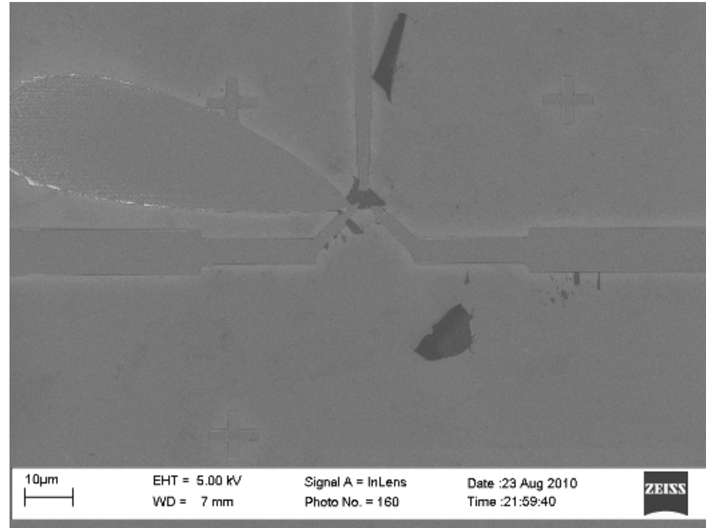

Figure 29: *SEM image of Ti/Au metal lines deposited on a MLG flake*

blow-drying. As impurities in resist can cause incomplete lift-off or breaks in thin metallic lines the surface was checked to ensure homogeneous and continuous metal deposition. A SEM image of the effects of incomplete lift-off process can be seen in Fig. 29. Luckily, in this case there were no visual evidence of metallic remains on the graphene flake and it could be used for the subsequent etching stage.

For this stage, a dual layer of resist was again spin-coated on the substrate. This time however, PMMA was deposited before MMA. At each resist deposition stage the substrate was spun at 4000 rpm for 60 seconds, and, then left on a hot-plate at 170°C for 5 minutes. The longer pre-baking time ensured thinner resist layer heights, thereby reducing bias introduced due to scattering by secondary electrons during exposure. PMMA being less soluble in developer than MMA, and hence, offering significantly better resolution, was used as the first layer in this highly sensitive stage. Exposure was done with a beam acceleration voltage of 30 kV and dose of 275 μC/cm^2. The dose was slightly less than the critical dose of PMMA at 30 kV, and was found out to give sharper edges after etching. Development was done in 1:3 MIBK:IPA solution kept at 9°C. Development is slightly slower at such reduced temperatures and ensures better vertical side-profile of resist. After the development process the substrate was put in a Plasmalab 80+ Reactive ion etcher, manufactured by Oxford Instruments Plasma Technology, for plasma etching.

Etching was done at a pressure of 250 mTorr with an operating power of 20 W and a mixture of oxygen and argon. A flow rate of 18 sccm for oxygen and 25 sccm

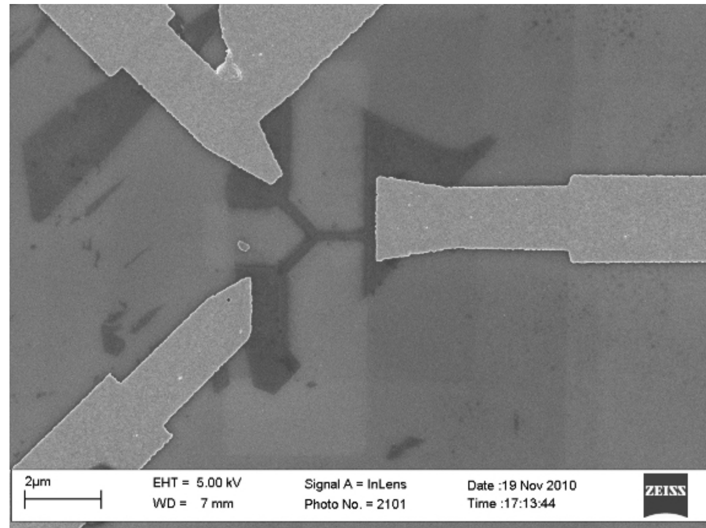

Figure 30: *SEM image of the MLG flake in the previous figure after etching*

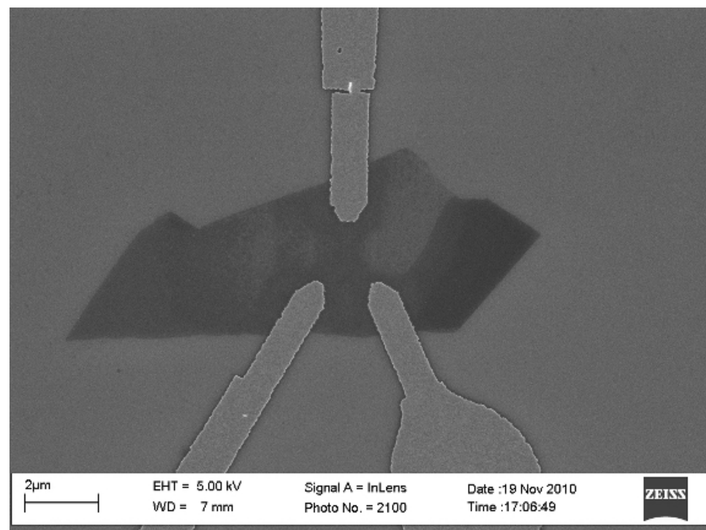

Figure 31: *SEM image of a BLG flake after etching for 90 seconds*

for argon was used - changing the flow rates to 45 sccm and 5 sccm respectively, gave significantly faster etch rates but unpredictable results. It was found out that the time required to etch through MLG was about 30 seconds. SEM image of a Y-branch fabricated on MLG can be seen in Fig. 30 - the geometry of the obtained device, in this case, is in accordance to what was intended, and the edges are more-or-less uniform. For BLG, however, the etching time was variable. An example is given Fig. 31 - the SEM image revealed large areas of unetched graphene even after etching for 90 seconds (in two steps of 60 seconds and 30 seconds, without any

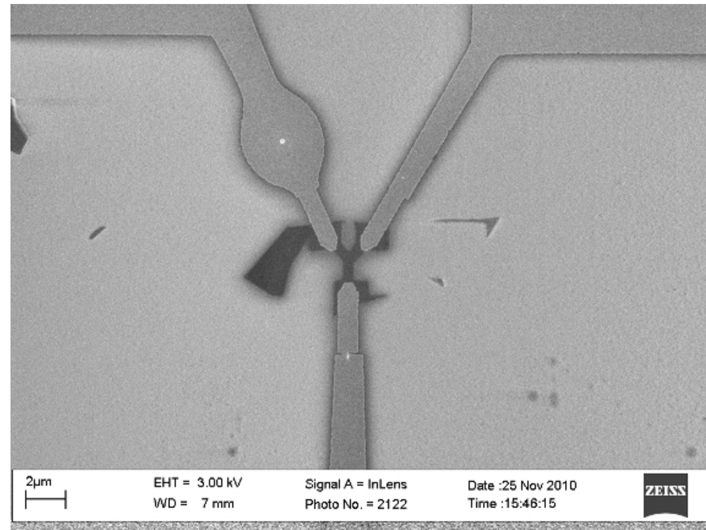

Figure 32: *SEM image of the BLG flake in the previous figure after further 30 seconds of etching*

nanolithographic processes in between). So the sample was subjected to a second round of exposure and etching for 30 seconds. Even after that, the dimension of the branches (SEM image in Fig. 32) were 300 nm and 1200 nm; further etching to reach the intended width of 200 nm was not attempted in this case. This is because each iteration of etching process requires additional nanolithographic stages and increase chances of contamination.

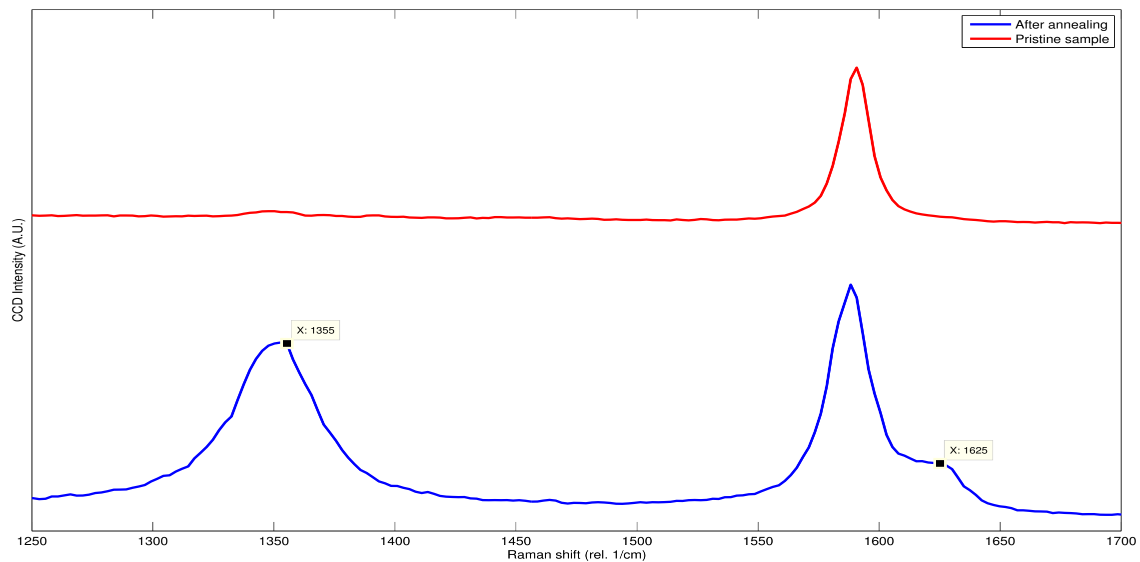

Figure 33: *Raman signature of a MLG flake before and after annealing*

After RIE, the resist was removed by treatment in hot acetone (70°C) for 15 minutes, followed by rinsing in IPA and DIW and nitrogen blow-drying. Thereafter, the samples were annealed in a Plasmalab 80+ PECVD, manufactured by Oxford Instruments Plasma Technology. Annealing was done at 300°C for 15 minutes, under nitrogen gas with a flow rate of 1000 sccm and an operating pressure of 200 mTorr. The effect of fabrication and annealing was studied with Raman spectroscopy. As can be seen from Fig. 33 the Raman signature of the fabricated sample is different from that of a pristine MLG. It shows a peak at 1355 cm^{-1} (D line) indicating damage to the crystal, and, a band at 1625 cm^{-1}, probably due to doping.

5 Measurement and discussion

Having obtained three terminal junctions on graphene the next step is electrical characterisation of the devices. Measurements were carried out on both MLG and BLG samples shown in Fig. 30 and Fig. 32 respectively. Unfortunately, the MLG sample was damaged during measurement; some of the data for MLG sample presented here was the result of measurements carried out on a similar sample provide for kindly by my thesis instructor. The device geometry precluded the possibility of simultaneous application and measurement of voltage/current signal at a particular contact. The irregular shape of the contacts also ruled out any meaningful approximation of the contact resistance. These limitations rendered conductivity measurements impossible; observation and analysis had to be restricted to I-V measurements.

5.1 Measurement results

Electrical characterisation of the graphene nano-junction was conducted in a probe station equipped with a Hewlett-Packard 4155A semiconductor parameter analyser. The probes attached to the analyser allowed for application of a voltage signal and simultaneous measurement of current flowing through it (and, vice versa). A schematic of the measurement setup is shown in Fig. 34. As can be seen from the figure, contact with the three branches of the device were made by directly pressing

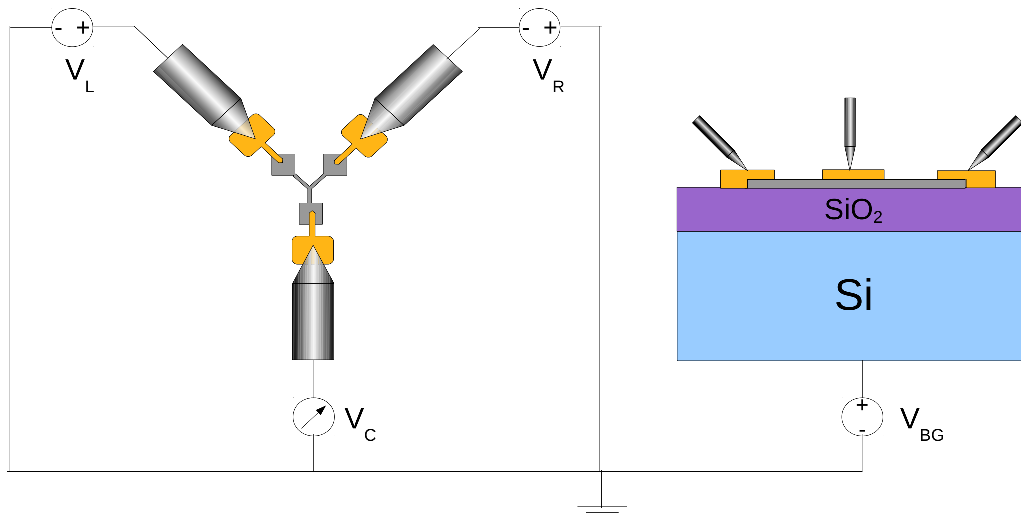

Figure 34: *Schematic of measurement setup*

the metallic probe onto the metallic pad connected to the respective branch. The back-gate voltage was provided for by pressing another probe onto the metallic chuck on which the sample chip was put; to facilitate the connection the backside of the chip was coated with a conductive gallium-based fusible alloy. For the ease of reference the voltage or current signal, applied to, or detected at, any branch of the device would be referred to as V_i or I_i, where, $i = L, R\ or\ C$. All measurements were carried out at room temperature.

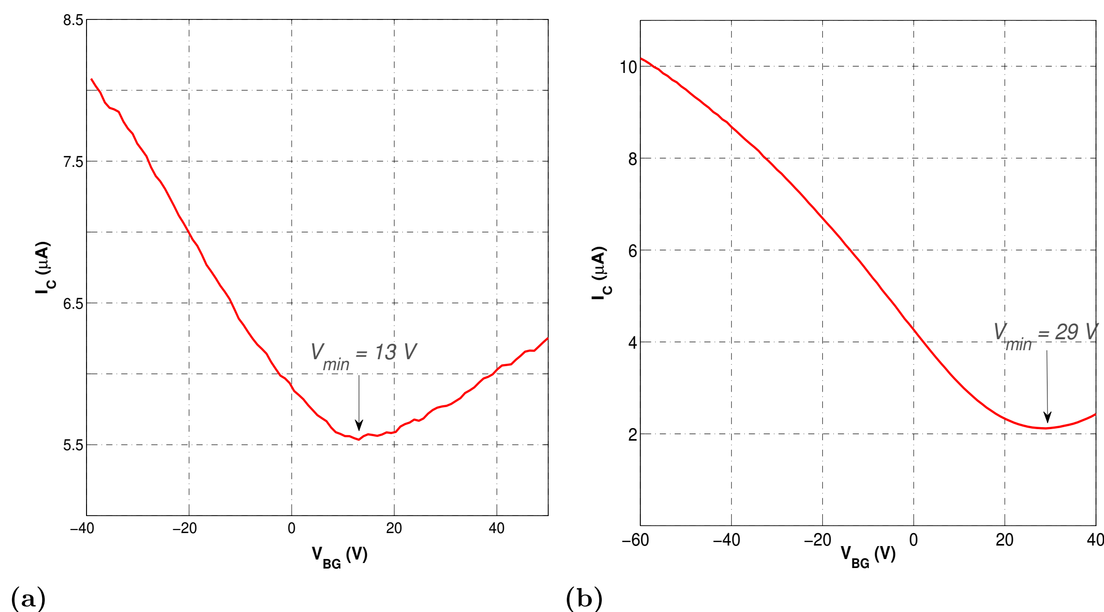

Figure 35: *I_C vs V_{BG} graph for a.MLG, and, b.BLG device*

The first set of observations were directed toward finding out the change in conductivity of graphene with the application of back-gate voltage. For this set of measurement V_L and V_R were set to 100 mV and 0 mV respectively, while V_{BG} was varied from −60 V to +60 V. The detected output I_C was then plotted against V_{BG}; with a constant applied bias, the change in I_C was the best available parameter to analyse the change in conductivity of graphene. The obtained results for the MLG and the BLG sample are shown in Fig.35a and Fig.35b respectively. Both of them exhibit the familiar ampbipolar character of graphene. The obtained CNP (indicated in the figures as V_{min}) for MLG and BLG are at 13 V and 29 V respectively. For $V_{BG} > V_{min}$ the device would be in the electron transport regime, and, For $V_{BG} < V_{min}$ the device would be in the hole transport regime. For both samples, V_{min} is greater than zero - this indicates strong p-doping. As has been mentioned in

Sec. 3.3.3 this doping is an inadvertent result of the fabrication process and exposure to the ambient after the final annealing step.

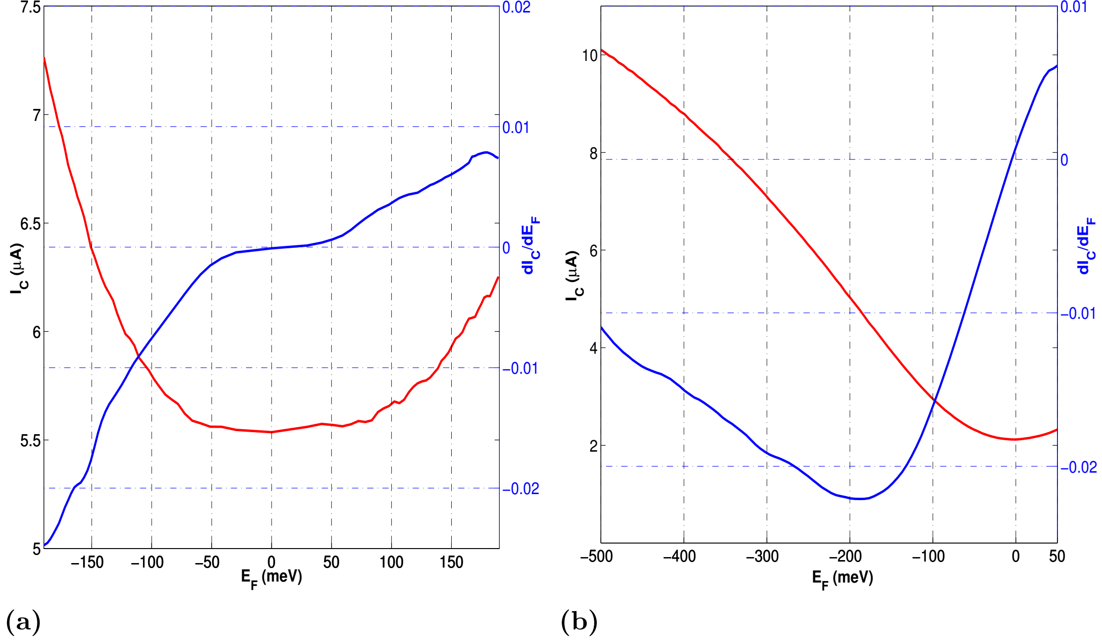

Figure 36: *I_C vs E_F graph for a.MLG, and, b.BLG device*

A better way to analyse the ambipolar nature of graphene would be to plot conductivity (or, in this case I_C) against the Fermi energy E_F of the system. It has already been mentioned in Sec. 2.1.1 that V_{BG} affects the carrier concentration n according to Eq. 6. This in turn changes E_F according to Eq. 7 (for MLG) or Eq. 8 (for BLG). As the devices under discussion are constituted of extrinsic graphene the term V_{BG} in Eq. 6 should be replaced by $(V_{BG} - V_{min})$ to accommodate for the change in CNP. Substituting for the values of the parameter, the following simplified equations are obtained:

$$\textbf{MLG:} \qquad E_F = sgn(V_{bg} - 13)31.15\sqrt{|V_{bg} - 13|} \quad meV \tag{11}$$

$$\textbf{BLG:} \qquad E_F = 5.7(V_{bg} - 29) \quad meV \tag{12}$$

where, $sgn(x)$ is the signum function.

I_C and $\delta I_C/\delta E_F$ were plotted against E_F for both MLG and BLG. For BLG, $E_F \propto V_{BG}$ and the graph for I_C vs E_F in Fig. 36b is quite similar to that of I_C

vs V_{BG}. It can also be observed from the same figure that $\delta I_C/\delta E_F$ (and hence, $\delta G/\delta\mu$) is greater than zero when $E_F > 0\ meV$ (i.e., $V_{BG} > 29\ V$), and vice-versa. For MLG, however, the dependence between E_F and V_{BG} is non-linear and the graph for I_C vs E_F in Fig. 36a exhibits one striking difference from that of I_C vs V_{BG}. There is a minimum conduction plateau from about -50 meV to $+50$ meV (corresponding to V_{bg} of 0 V to 16 V) where I_C remains more or less constant at 5.56 μA. It has already been argued in Sec. 2.1.1 that this is a direct result of the long range Coulomb scatterers. Furthermore, Fig. 36a also shows that for MLG, $\delta I_C/\delta E_F$ is approximately zero in the MCP, greater than zero for $E_F > 50\ meV$ (i.e.,$V_{BG} \gtrapprox 16\ V$) and less than zero for $E_F < -50\ meV$ (i.e., $V_{BG} \lessapprox 10\ V$). Additionally, $\delta I_C/\delta E_F$ decreases much more rapidly in the hole transport regime than it increases in the electron transport regime - this might again be a result of p-doping of the MLG.

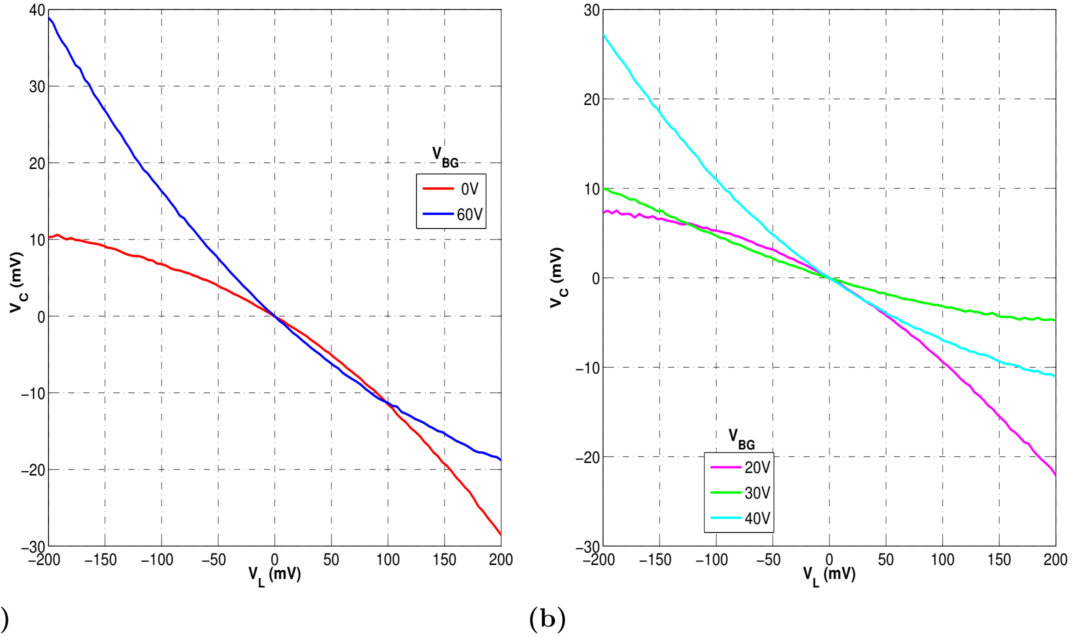

Figure 37: *Output curve for BLG device in push-pull configuration with V_{BG} set a.far away from, and, b.near the CNP*

For the purpose of measuring the behaviour of devices under push-pull configuration V_L was varied from -200 mV to $+200$ mV, while keeping $V_R = -V_L$. The output voltage V_C was then plotted against V_L ; different values of V_{BG} were chosen to observe device operation near, as well as far away, from the CNP. Results for the BLG device functioning far away from CNP (by setting V_{BG} equal to 0 V and 60 V) is seen in Fig. 37a, whereas those for device functioning near CNP (by setting V_{BG}

equal to 20 V, 30 V and 40 V) is presented in Fig. 37b. The output, for all values of V_{BG} is, to a degree non linear, though perhaps not about the x-axis.

The extent to which the curves are non linear depend prominently on applied V_{BG}. When the device was made to operate deep into the hole transport regime by setting $V_{BG} = 0\ V$ ($E_F = -165.3\ meV$), the obtained output curve bend downward. Operating it at an almost equal distance into the electron transport regime by setting $V_{BG} = 60\ V$ ($E_F = +175.7\ meV$) caused the output to bend upward. When $V_{BG} = 20\ V$ ($E_F = -51.3\ meV$) the output curve bends downward, whereas setting $V_{BG} = 40\ V$ ($E_F = +62.7\ meV$) the output curve bends upward. However, compared to the curves in Fig. 37a, those in Fig. 37b are distinctly flatter. Comparing these plots with Fig. 6b indicate that the tilting of axis might be due to asymmetry between the left and right branches of the device. Interestingly, at $V_{BG} = 30\ V$ ($E_F = +5.7\ meV$), when the device is operating very close to the CNP, the curvature of the output decreases drastically.

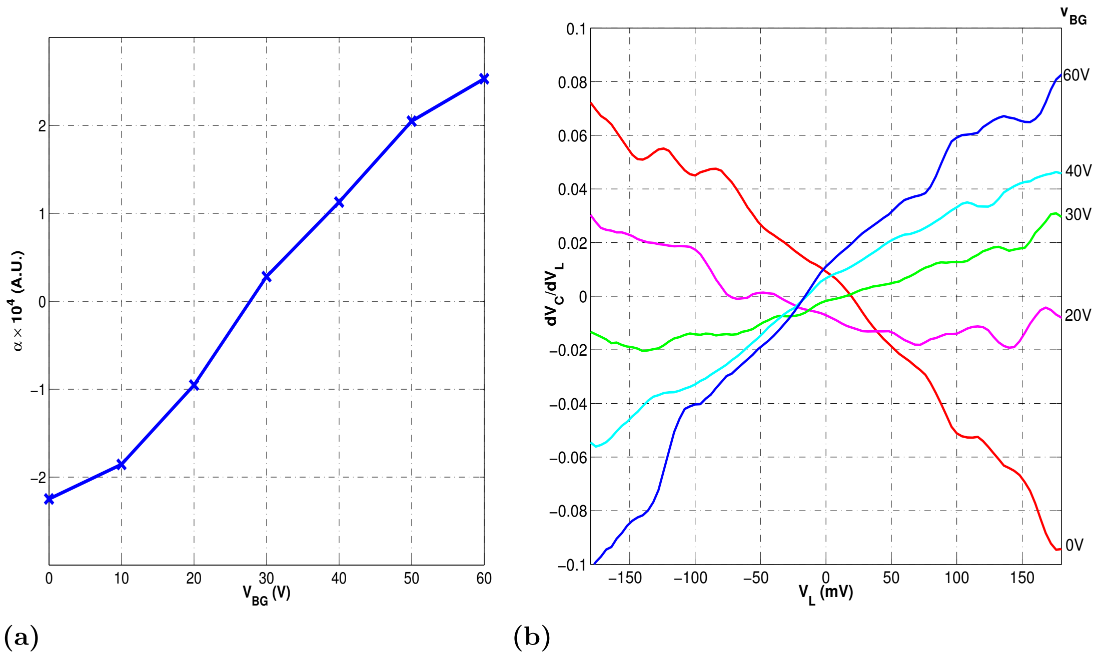

Figure 38: *a. Second order coefficient obtained from a fit of the push-pull data of BLG plotted against V_{BG}; b. $\delta V_C/\delta V_L$ vs V_L for push-pull measurements on BLG*

In order to get a closed form mathematical expression for the output data, the V_C vs V_L curves were fit to polynomial equations. A third degree polynomial with a large first order coefficient and a very small third order coefficient gave the best fit for all output curves. The second order coefficient was found out to be a

good representative of the curvature of the output. Following the convention set in Sec. 2.3.1 this coefficient can be referred to as α. The values of α obtained from a cubic fitting of output curves corresponding to different V_{BG}, is plotted against V_{BG} in Fig. 38a. As can be seen from the plot, α is negative for $V_{BG} < V_{min}$ (implying, $E_F < 0$ and from Fig. 36b $\delta I_C/\delta E_F < 0$) and positive for $V_{BG} > V_{min}$ (i.e., $E_F > 0$ and $\delta I_C/\delta E_F > 0$). This is an affirmation of the fact that the output curve bends downward for hole dominated transport, and upward for electron dominated transport. Furthermore, it is also observed that the magnitude of α increases as $|V_{BG} - V_{min}|$ increases. Thus, the effect of increasing V_{BG} within a particular transport regime is a progressive strengthening of the curvature of the output.

A further confirmation of this behaviour comes from Fig. 38b which plots $\delta V_C/\delta V_L$ against V_L. Owing to the noise in the V_C curve, the $\delta V_C/\delta V_L$ curves are quite irregular. Nevertheless all of them tend to be linear for the entire range of applied V_L; this suggests that the actual outputs were parabolic in nature and were non linear for all values of input voltage. The slope of the $\delta V_C/\delta V_L$ curve when V_{BG} is equal to 20 or 30 or 40 V is visibly lesser than when V_{BG} is set to 0 or 60 V. This proves unambiguously that the output curve becomes more non-linear as the device is made to operate further away from the CNP. It is also worth noting that the slopes are positive in the electron transport regime, and negative in the hole transport regime.

For testing the MLG device a configuration similar to the BLG device was chosen. As can be seen in Fig. 39a, for $V_{BG} = -20\ V$ ($E_F = -178.94\ meV$) the output curve bends downward, whereas for $V_{BG} = 50\ V$ ($E_F = +184.48\ meV$) the output curve bends upward, albeit less prominently. The curves are again non linear, but not about the x-axis. Thus, qualitativelt both MLG and BLG device have the same output behaviour when operated far away from the CNP. To test the output behaviour close to the CNP four values of V_{BG} were chosen: two of them at the edge of the MCP and two away from it. The results are shown in Fig. 39b. When V_{BG} was equal to 10 V ($E_F = -53.95\ meV$) or 20 V ($E_F = +82.42\ meV$), i.e., the device was operated at the edge of the MCP, the output becomes almost linear. When the device was operated slightly away from the MCP, by setting V_{BG} equal to 0 V ($E_F = -112.31\ meV$) or 30 V ($E_F = +128.43\ meV$) the output becomes non linear. The curves, as seen in Fig. 39b are distinctly flatter than those in Fig. 39a. While the curve for $V_{BG} = 0\ V$ distinctly bends downward, the one for $V_{BG} = 30\ V$ is only slightly non linear.

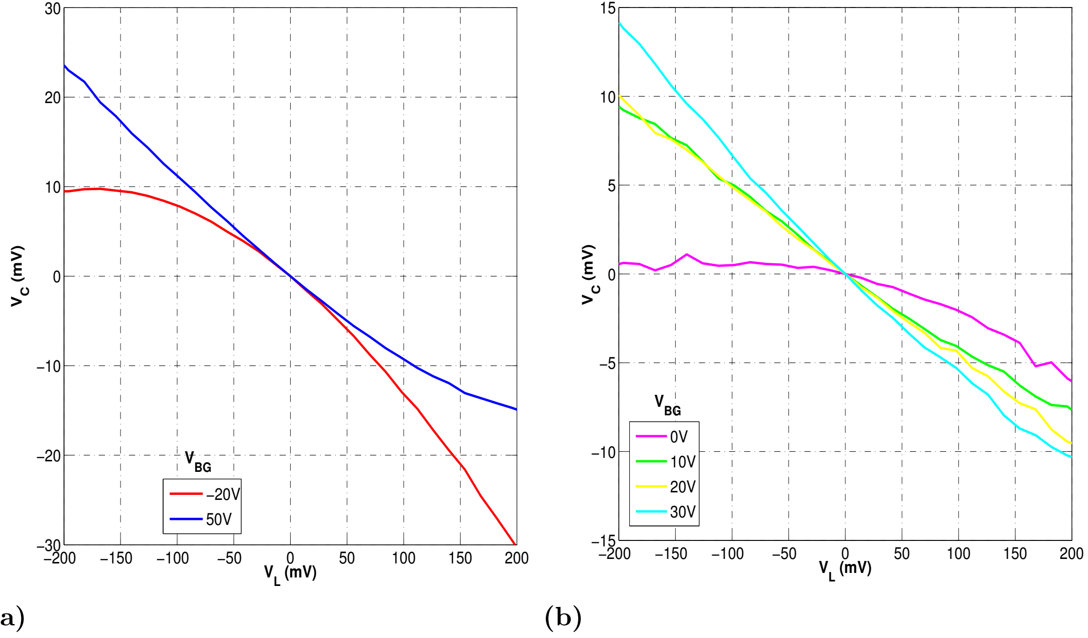

Figure 39: *Output curve for MLG device in push-pull configuration with V_{BG} set a.far away from, and, b.near the CNP*

Each of the obtained output curves for MLG were fitted to a cubic polynomial. Values of the second-order coefficient derived thereof is plotted against V_{BG} in Fig. 40a. Additionally, results of plot between $\delta V_C/\delta V_L$ and V_L is shown in Fig. 40b. Both of these curves show a a trend similar to that of BLG. Interestingly, for V_{BG} equal to 10 V or 20 V, the values of α and $\delta V_C/\delta V_L$ are almost equal to zero . This shows that when the MLG device is operated at, or very near to the MCP, the push-pull output is still linear. The metrics, i.e., magnitude of α and the slope of $\delta V_C/\delta V_L$ becomes larger as the device is operated farther away from the MCP. The metrics for V_{BG} equal to -20 V or 0 V (in the hole transport regime) are visibly larger in magnitude than the ones when the device is operated with V_{BG} equal to 30 V or 50 V (in the electron transport regime). This behaviours suggests that $|\alpha|$ is linked to $\delta I_C/\delta E_F$. As was as seen in Fig. 36a, $\delta I_C/\delta E_F$ is zero in the MCP, and its magnitude increased faster in the hole transport regime than in the electron transport regime - the same trend is also seen in $|\alpha|$. Also noticeable from these curves is the change in sign of the metrics when device operation is switched from electron dominated to hole dominated transport regime.

To analyse the dependence of output curve on the degree of imbalance between two branches, measurements were repeated with $V_R = 0.8 \times V_L$ for the BLG bsed

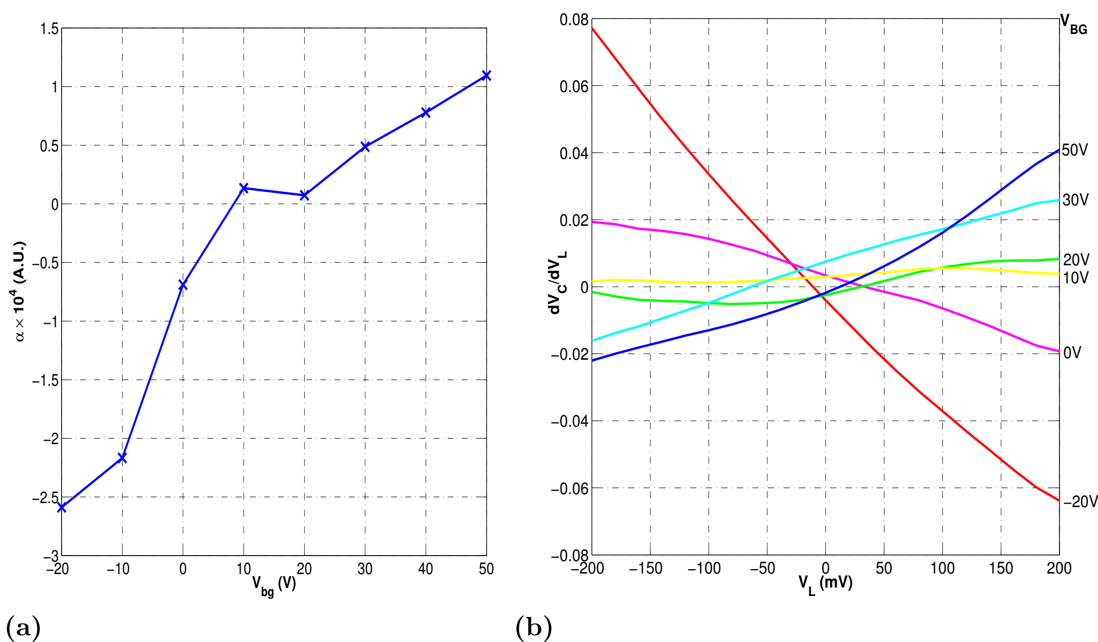

(a) **(b)**

Figure 40: *a. Second order coefficient obtained from a fit of the push-pull data of MLG plotted against* V_{BG} *;b.* $\delta V_C/\delta V_L$ *vs* V_L *for push-pull measurements on MLG*

device and with $V_R = 0.9 \times V_L$ for the MLG based device. The output data is given in Fig. 41a and Fig. 41b for the BLG and the MLG based device, respectively. From the output data for BLG, it can be inferred that the imbalance in electrical input has offset the ones in the structure. The output curves for $V_{BG} = 0\ V$ and $V_{BG} = 60\ V$ are parabolic and nicely symmetrical along the x-axis. The curve for $V_{BG} = 30\ V$ is almost linear and amplifies the electrical imbalance between branches. The output data for MLG reveal a general increase in non linearity, especially when device was operated far away from CNP. The output curves for device operated at the edge of MCP remained linear.

The measuring apparatus allowed for detection of the current flowing through the branches while operating the devices in push-pull configuration. For all measurements, I_C was predictably, zero. The current through the other two branches increased linearly with the voltage applied to that branch. This can be clearly seen in Fig. 42a and Fig. 42b which shows I_L vs V_L curves for different V_{BG} in the BLG and MLG sample, respectively. For both MLG and BLG sample, the current is higher in magnitude while operating away from the CNP. Furthermore, the current is higher when the devices are operating in the hole transport regime. Both of these observations are predictable - the magnitude of the current ultimately depends upon

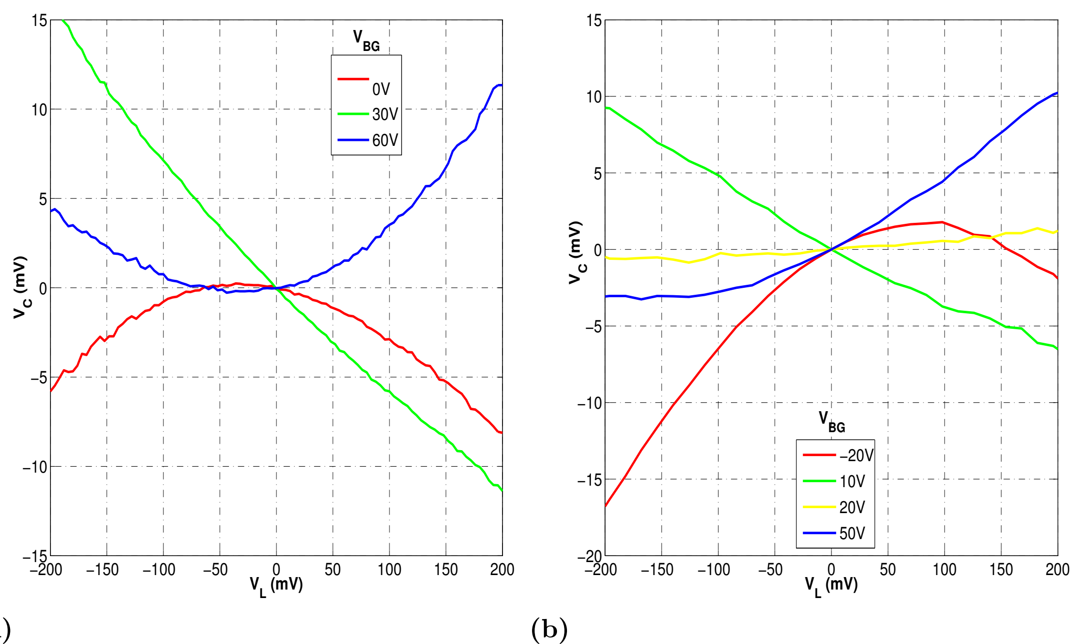

Figure 41: *Study of effect of asymmetrical bias: a. Output curves obtained from BLG device for* $V_R = 0.8 \times V_L$*; b.Output curves obtained from MLG device for* $V_R = 0.9 \times V_L$

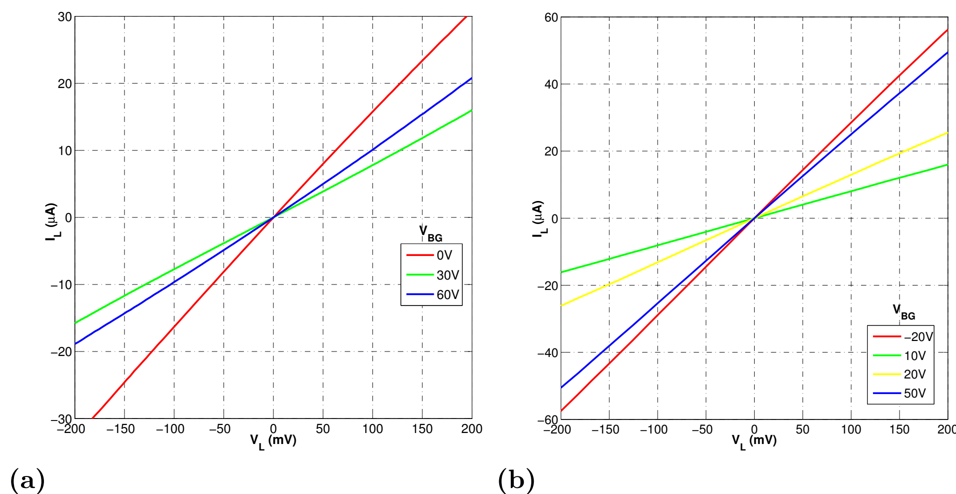

Figure 42: I_L *vs* V_L *curve obtained during push-pull measurements on a.BLG, and, b.MLG device*

the concentration of charged carriers in the system.

Both devices also displayed some degree of current rectification. The devices were again operated in a push-pull configuration, but instead of V_C, it was the current through the central branch, I_C that was detected. Graphs obtained by plotting I_C

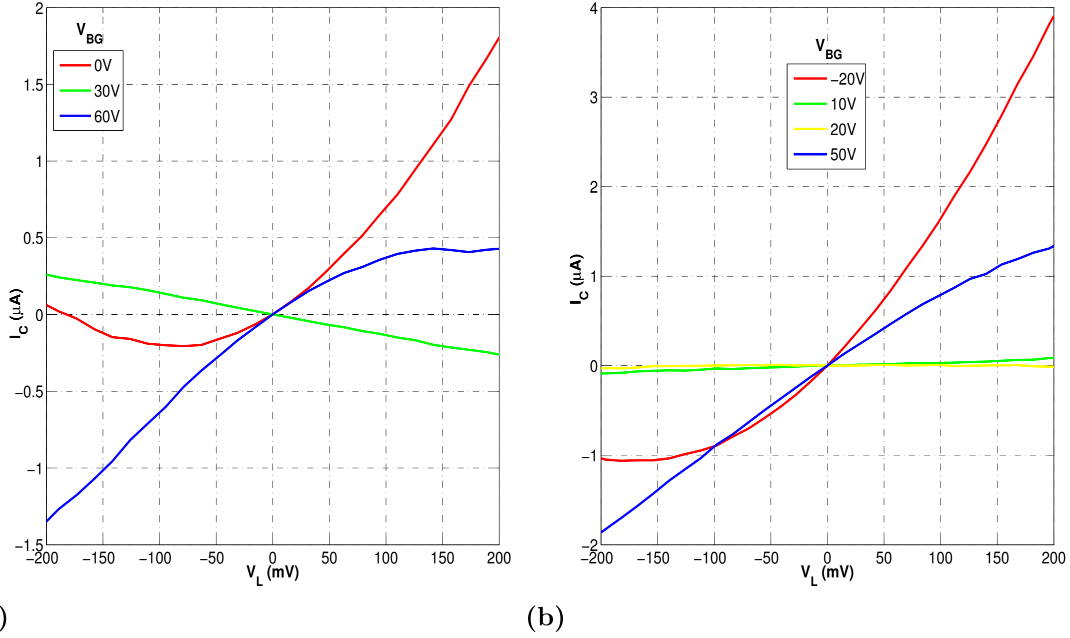

(a) **(b)**

Figure 43: *Curves for output current obtained with push-pull measurements on a.BLG, and, b.MLG device*

against V_L is shown in Fig. 43a for the BLG sample and in Fig. 43b for the MLG sample. For the BLG sample, the output curves for V_{BG} equal to 0 V and 60 V are markedly non linear. When $V_{BG} = 30\ V$, i.e., the device is operated near to the CNP, the output is linear. Similarly, for the MLG sample, the obtained output curves are linear when the device is operated at the edge of MCP (when V_{BG} is equal to 10 V or 20 V), and non-linear otherwise (when V_{BG} is equal to -20 V or 50 V). For both devices, output remains very low for operation near the CNP; it is almost zero for the MLG sample. The output curves for current measurement also show the effect of imbalance observed in voltage measurements.

This concludes the section on measurement results. In a nutshell, the data can be summarised as follows: in a push-pull configuration, a non linear output is obtained from both MLG and BLG device. The degree of non linearity, α is positive for $\delta I_C/\delta E_F > 0$, and vice-versa. Also, $|\alpha|$ increases with $|E_F|$ and as observed from the data corresponding to MLG device, is correlated to $\delta I_C/\delta E_F$. The next section will explain these salient points in slightly greater detail, in light of earlier observations furnished in Sec. 2.3.2. An effort would also be made to explain the behaviour according to the theoretical knowledge developed in Sec. 2.1.1 and 2.3.1.

5.2 Discussion

Measurement data presented in the last section clearly shows that the voltage or current output from a graphene based three terminal junction operating in push-pull configuration, is non linear for the entire range of input voltage. Unlike the output curves demonstrated on semiconductor heterostructure (refer Sec. 2.3.2) the ones obtained here are not symmetrical across the x-axis. This anomaly could be attributed to a probable mismatch in the dimensions of the left and right terminal of the devices. SEM images of the MLG and BLG shown in Sec. 4.3 indicate that the mismatch arose due to the irregular shape of the area where the metal contacts meet graphene.

In spite of the irregularity of the output curves, qualitatively, they are parabolic for the entire range of input. This is confirmed by the dominance of the second order coefficient in the cubic fit of the $V_C/;vs/;V_L$ curves and the fact that the slope of the output curves are linear for the full input range. Moreover, the curves obtained by biasing the left and branches asymmetrically are distinctly parabolic. Hence, it would be reasonable to conclude that the output obtained from a balanced three terminal junction would be parabolic, and symmetric along the x-axis.

The observations also indicate that the output of the device is intricately linked to the applied back-gate voltage. When the applied V_{BG} is such that electrons are majority carriers in the device, the output curve tends to bend upward. For a symmetrical device this would mean that the output would be positive for the applied input voltage. Similarly, in the hole transport regime, the output curve tends to bend downward; for a balanced device the output would be negative for the entire range of input voltage. This observation is in direct contradiction with those obtained in [8]. Their output data, as seen in Fig. 8b, indicates the exact opposite! A further contradiction comes from the way the output behaves when the device is made to operate progressively deeper into a particular transport regime. From the voltage output measured in this thesis, it is seen that the output curve becomes more and more non linear as V_{BG} is moved away from the CNP. The data reported in [8] suggests that under these conditions the curves should become weaker.

These two observations also contravene the theoretical prediction and experimental proves thereof presented in Sec. 2.3. These anomalies forced repetition of the entire gamut of measurement. However, other than a degradation in quality of output curves, possibly due to ageing of contact material, no significant differences

were noticed. Hence, within the limit of the observed data the anomalies can be reconciled with the earlier, published results as follows: the results given in [8] were obtained from a three terminal nano-constriction, not from a more traditional Y-branch device, as was done in this thesis. The conflict with the results obtained for heterostructure based three terminal junctions might be attributed to a difference in the underlying mechanism.

It must be said that, at this point, the physics behind the output behaviour is not well understood. One thing can be said with certainty - the transport in the graphene devices is not ballistic. As was pointed out in Sec. 2.2 ballistic transport can only be observed in suspended graphene. This rules out the possibility of explaining the behaviour in terms of the model proposed in [7] - the devices used in this thesis were based on supported graphene. Ballistic behaviour due to bias induced enhancement of mean free path can also be ruled out. As was pointed out in Sec. 2.3.2, this mechanism entails appearance of a linear segment in the voltage output [34]. The output, as observed in this thesis, remained non linear for the entire range of operation. The justification furnished for non linear output from graphene device in [8] cannot be used as the output data is the complete opposite of what has been measured in here. Additionally, their explanation seems to suggest that the effect on the conductance of a branch would be the same for the two contrasting cases: the applied back gate voltage is changed with a constant bias, and, the bias is changed with a constant back gate voltage. Although, conceptually this is an attractive way of explaining the phenomenon in terms of difference in conductivity between the two input terminals and the central one, the lack of any analytical expression prevented the extension of this schematic to the geometry, and hence the output behaviour of the device discussed in this thesis.

The only way to obtain an analytical explanation for the behaviour would probably be a bottoms-up approach starting from the basic transport properties of graphene. This can be done in either of two ways. The first one is based on transmissivity calculations [66]. Though, there have been some studies on multi terminal graphene junction based on this approach , e.g. [67, 68] the investigation was based on GNR. The other approach is of course based on the drift-diffusion approach used to explain behaviour of traditional silicon MOSFET devices. There have been some recent studies based on this approach which show inhomogeneous charge distribution in a straight graphene sheet [69, 70]. It remains to be seen whether these principles can be extended to a three terminal, Y-shaped device based on graphene.

Before concluding the discussion of the results obtained here, it would be imperative to quote and compare the performances of the MLG and BLG based devices. The irregular shape of the output makes direct comparison a bit difficult. However a qualitative comparison can be made by utilising the cubic fit of the measured data, more specifically by retaining only the second order term from the fit. Under this assumption, it was found out that for operation away from CNP at comparable V_{BG}, the output from both MLG and BLG varies between 0% and $\sim 5\%$ of the input. For operation near CNP at comparable V_{BG}, the output for BLG is at its maximum equal to $\sim 3\%$ of input, whereas for MLG it is $\sim 2\%$. Though, the data set is too small and limited to give a firm comment upon the relative efficiency of either class of device, from the obtained measurements it can be said that the BLG device showed better rectifying properties in the electron transport regime and close to the charge neutrality point.

5.3 Future outlook

In view of the irregular output obtained from the devices due to the imbalance in left and right terminal, the first task would be to come up with better fabrication strategies to ensure proper balancing of the branches in a repeatable, unambiguous way. A bigger challenge would of course be to improve the structure so that it allows for elimination of the effects of contact resistance. This would also enable measurement and analysis of conductance of individual branches. Both of these aims can be achieved by reducing the ratio of the size of the active device and the graphene flake on which it is fabricated. Finally, using a top gate structure instead of the back gate configuration used here would make actual circuit realisation easier by eliminating the need to employ high voltages to achieve the ambipolar effect in graphene.

From a theoretical point of view, a deeper understanding of the physics behind the operation of three terminal graphene junction is of utmost importance. In this respect low temperature measurement of the devices might give some valuable insight. To test the role of ballistic transport in the scheme, devices based on suspended graphene can also be fabricated and investigated into. Finally, a detailed study of the dependence of output curve on the size, included angle and width vs length ratio of T and Y-shaped branches fabricated on graphene would be desirable.

6 Conclusion

Graphene, a newly discovered allotrope of carbon is poised to take the scientific world by storm. Its unique electronic structure makes it a perfect candidate for experimental observation of many new physical phenomenon and making forays into high-speed, low-power electronics, thereby continuing the breath-taking pace at which the electronics industry has been expanding over the last few decades. Of particular importance are the high mobility of charge carriers and the ability to tune the nature of charge carriers from electron to hole using an external electric field. Unfortunately the lack of band gap in graphene also means that traditional device structures cannot be used to make useful electronic components from graphene. However, a novel structure known as three-terminal ballistic junctions, which show non-linear electrical properties for a wide range of temperature, provide a way to exploit the 'useful' properties of graphene. It was the aim of this thesis to verify if this is indeed possible.

To this end graphene was synthesised and deposited on a silicon dioxide substrate (the dioxide layer was obtained by thermal growth on a silicon chip) using micro-mechanical cleavage method employing a scotch-tape and graphite. The graphene flakes thus obtained were characterised using optical microscopy, atomic force microscopy and Raman spectroscopy; single and two layer graphene flakes were isolated from flakes with greater number of layers. Nanolithographic techniques were used to etch out nanoscale, Y-shaped structures out of both MLG and BLG flakes. Microfabrication techniques were used to deposit Ti/Au metal contacts to facilitate electrical measurement of the devices.

Measurement was carried out at room temperature with a push-pull configuration. It was found out that when equal and opposite voltage is impressed upon the left and right arm of the devices, the output from the central branch, be it voltage or current, is non linear for the entire input range. Due to an asymmetry between the left and right terminal of both devices the obtained was not symmetrical along the x-axis. Fitting the output curve to a third degree polynomial revealed that the output is largely parabolic.

Due to the ambipolar effect of graphene, the nature of the output curve could be tuned by applying a back-gate voltage to the devices. More specifically, the non-linearity factor of the voltage output curves, α was found out to be dependent upon $\delta I_C/\delta E_F$. The latter factor was calculated by varying the back gate voltage while

applying a constant bias to the device; this measurement also revealed that the charge neutrality point for both devices is reached for a positive V_{BG}. It was found out that when the applied V_{BG} causes the device to operate in electron transport regime (under this condition, the Fermi level E_F of the system is greater than zero, i.e. it is in the conduction band) both $\delta I_C/\delta E_F$ and α are positive. The voltage output curves under this situation were inclined upwards. The exact opposite behaviour was observed while operating the device in the hole transport regime, i.e., for $E_F < 0$, both $\delta I_C/\delta E_F$ and α are negative and the output curves were inclined downward.

It was also observed that within a transport regime, moving the back gate voltage away from the neutrality point causes the output curve to become more and more non linear. The obtained output data from MLG based device also suggested a correlation between the magnitudes of α and $\delta I_C/\delta E_F$. Both of these observations are in direct contradiction with the results published in earlier literature. However, due to a lack of clear understanding of the physics underlying the operation, the anomaly could not be resolved completely. The efficiency of voltage rectification for both MLG and BLG based devices were found out to be $\sim 5\%$. It can be anticipated that with improvement of fabrication techniques and a clearer insight into the physics of operation, the bottle necks faced in this thesis would be removed. This would pave the way for a slew of electronic components like rectifiers, frequency multipliers, logic gates, diodes, transistors etc., all capable of performing at very high frequency, with a low power consumption.

References

[1] G. E. Moore, "Cramming more components onto integrated circuits," *Electronics*, vol. 38, no. 8, April 1965.

[2] K.S.Novoselov, A.K.Geim, S. Morozov, D. Jiang, Y. Zhang, S. Dubonos, I. Grigorieva, and A. Firsov, "Electric field effect in atomically thin carbon films," *Science*, vol. 306, no. 5696, pp. 666–669, 2004.

[3] M. I. Katsnelson, "Graphene: Carbon in two dimension," *Materials Today*, vol. 10, no. 2, pp. 20–27, 2007.

[4] A. K. Geim and K. S. Novoselov, "The rise of graphene," *Nature*, vol. 6, pp. 183–190, March 2007.

[5] A. Geim, "Graphene: Status and prospects," *Science*, vol. 324, no. 5934, pp. 1530–1534, 2009.

[6] M. Allen, V. Tung, and R. Kaner, "Honeycomb carbon: a review of graphene," *Chemical reviews*, vol. 110, no. 1, pp. 132–145, 2009.

[7] H. Q. Xu, "Electrical properties of three-terminal ballistic junctions," *Applied Physics Letters*, vol. 78, no. 14, pp. 2064–2066, 2001.

[8] A. Jacobsen, I. Shorubalko, L. Maag, U. Sennhauser, and K. Ensslin, "Rectification in three-terminal graphene junction," *Applied Physics Letters*, vol. 97, p. 032110, 2010.

[9] P. Wallace, "The band theory of graphite," *Physical Review*, vol. 71, no. 9, pp. 622–634, 1947.

[10] A. Neto, F.Guinea, N. Peres, K. Novoselov, and A. Geim, "The electronic properties of graphene," *Rev. Mod. Phys*, vol. 81, no. 1, pp. 109–162, 2009.

[11] S. Sarma, S. Adam, E. Hwang, and E. Rossi, "Electronic transport in two dimensional graphene," *arXiv:1003.4731*, (unpublished).

[12] N. Peres, "The electronic properties of graphene and its bilayer," *Vacuum*, vol. 83, no. 10, pp. 1248–1252, 2009.

[13] J. Chen, C. Jang, S. Adam, M. Fuhrer, E. Williams, and M. Ishigami, "Charged-impurity scattering in graphene," *Nature Physics*, vol. 4, no. 5, pp. 377–381, 2008.

[14] N. Peres, "Colloquium: The transport properties of graphene: An introduction," *Reviews of Modern Physics*, vol. 82, no. 3, p. 2673, 2010.

[15] E. Hwang, S. Adam, and S. Das Sarma, "Carrier transport in two-dimensional graphene layers," *Physical review letters*, vol. 98, no. 18, p. 186806, 2007.

[16] C. Lee, X. Wei, J.W.Kysar, and J. Hone, "Measurement of the elastic properties and intrinsic strength of monolayer graphene," *Science*, vol. 321, no. 5887, pp. 385–388, 2008.

[17] F. Bonaccorso, Z. Sun, T. Hasan, and A. Ferrari, "Graphene photonics and optoelectronics," *Nature Photonics*, vol. 4, no. 9, pp. 611–622, 2010.

[18] X. Li, X. Wang, L. Zhang, S. Lee, and H. Dai, "Chemically derived, ultrasmooth graphene nanoribbon semiconductors," *Science*, vol. 319, pp. 1229–1232, 2008.

[19] Y. Zhang, T.-T. Tang, C. Girit, Z. Hao, M. C. Martin, A. Zettl1, M. F. Crommie1, Y. R. Shen1, and F. Wang, "Direct observation of a widely tunable bandgap in bilayer graphene," *Nature*, no. 459, pp. 820–823, 2009.

[20] Y. Lin, K. Jenkins, A. Valdes-Garcia, J. Small, D. Farmer, and P. Avouris, "Operation of graphene transistors at gigahertz frequencies," *Nano Lett*, vol. 9, no. 1, pp. 422–426, 2009.

[21] D. Dikin, S. Stankovich, E. Zimney, R. Piner, G. Dommett, G. Evmenenko, S. Nguyen, and R. Ruoff, "Preparation and characterization of graphene oxide paper," *Nature*, vol. 448, pp. 457–460, 2007.

[22] F. Schedin, A. K. Geim, S. V. Morozov, D. Jiang, E. H. Hill, P. Blake, and K. S. Novoselov, "Detection of individual gas molecules absorbed on graphene," *Nature Materials*, vol. 6, pp. 652–655, 2007.

[23] J. S. Bunch, A. M. van der Zandeand Scott S. Verbridge, I. W. Frank, D. M. Tanenbaum, J. M. Parpia, H. G. Craighead, and P. L. McEuen, "Electromechanical resonators from graphene sheets," *Science*, vol. 315, no. 5811, pp. 490–493, 2007.

[24] S. Datta, *Electronic transport in mesoscopic systems.* Cambridge Univ Pr, 1997.

[25] C. Beenakker and H. van Houten, "Quantum transport in semiconductor nanostructures," *Solid state physics*, vol. 44, pp. 1–228, 1991.

[26] J. Chen, C. Jang, S. Xiao, M. Ishigami, and M. Fuhrer, “Intrinsic and extrinsic performance limits of graphene devices on sio2,” *Nature Nanotechnology*, vol. 3, no. 4, pp. 206–209, 2008.

[27] X. Du, I. Skachko, A. Barker, and E. Andrei, “Approaching ballistic transport in suspended graphene,” *Nature Nanotechnology*, vol. 3, no. 8, pp. 491–495, 2008.

[28] C. Gardes, Y. Roelens, S. Bollaert, J. Galloo, X. Wallart, A. Curutchet, C. Gaquiere, J. Mateos, T. Gonzalez, B. Vasallo *et al.*, “Ballistic nanodevices for high frequency applications,” *International Journal of Nanotechnology*, vol. 5, no. 6, pp. 796–808, 2008.

[29] S. Bollaerta, A. Cappya, Y. Roelensa, J. Gallooa, C. Gardesa, Z. Teukama, X. Wallarta, J. Mateosb, T. Gonzalezb, B. Vasallob, B. Hackensca, L. Berdnarzc, and I. Huynen, “Ballistic nano-devices for high frequency applications,” *Thin Solid Films*, vol. 515, no. 10, pp. 4321–4326, 2007.

[30] A. Song, “Room-temperature ballistic nanodevices,” *Encyclopedia of Nanoscience and Nanotechnology*, vol. 9, no. 1, pp. 371–389, 2004.

[31] A. Jordan and M. Buttiker, “Gap theory of rectification in ballistic three-terminal conductors,” *Physical Review B*, vol. 77, no. 7, p. 075334, 2008.

[32] L. Worschech, H. Q. Xu, A. Forchel, and L. Samuelson, “Bias-voltage-induced asymmetry in nanoelectronic y-branches,” *Applied Physics Letters*, vol. 79, no. 20, pp. 3287–3289, 2001.

[33] K. Hieke and M. Ulfward, “Nonlinear operation of the y-branch switch: Ballistic switching mode at room temperature,” *Physical Review B*, vol. 62, no. 24, pp. 16 727–16 730, 2000.

[34] D. Wallin, I. Shorubalko, H. Xu, and A. Cappy, “Nonlinear electrical properties of three-terminal junctions,” *Applied physics letters*, vol. 89, no. 9, pp. 092 124–092 124, 2006.

[35] H. Irie, Q. Diduck, M. Margala, R. Sobolewski, and M. Feldman, “Nonlinear characteristics of T-branch junctions: Transition from ballistic to diffusive regime,” *Applied Physics Letters*, vol. 93, p. 053502, 2008.

[36] P. R. Bandaru, C. Daraio, S. Jin, and A. M. Rao, “Novel electrical switching behaviour and logic in carbon nanotube Y-junctions,” *Nature Materials*, vol. 4, no. 9, pp. 663–666, 2005.

[37] F. Meng, J. Sun, M. Graczyk, K. Zhang, M. Prunnila, J. Ahopelto, P. Shi, J. Chu, I. Maximov, and H. Xu, “Nonlinear electrical properties of Si three-terminal junction devices,” *Applied Physics Letters*, vol. 97, p. 242106, 2010.

[38] I. Shorubalko, H. Q. Xu, I. Maximov, D. Nilsson, R. Omling, L. Samuelson, and W. Seifert, “A novel frequency-multiplication device based on three-terminalballistic junction,” *IEEE Electron Device Letters*, vol. 23, no. 7, pp. 377–379, 2002.

[39] H. Q. Xu, “Diode and transistor behaviors of three-terminal ballistic junctions,” *Applied Physics Letters*, vol. 80, no. 5, pp. 853–855, 2002.

[40] H. Irie, “Ballistic electron transport in nanoscale three-branch junctions,” Ph.D. dissertation, University of Rochester, 2010.

[41] M. Dresselhaus and G. Dresselhaus, “Intercalation compounds of graphite,” *Advances in Physics*, vol. 30, no. 2, pp. 139–326, 1981.

[42] Y. Hernandez *et al.*, “High-yield production of graphene by liquid-phase exfoliation of graphite,” *Nat. Nanotechnol*, vol. 3, no. 9, pp. 563–568, 2008.

[43] K. Emtsev *et al.*, “Towards wafer-size graphene layers by atmospheric pressure graphitization of silicon carbide,” *Nature Materials*, vol. 8, no. 2, pp. 203–207, 2009.

[44] S. Park, J. An, I. Jung, R. Piner, S. An, X. Li, A. Velamakanni, and R. Ruoff, “Colloidal suspensions of highly reduced graphene oxide in a wide variety of organic solvents,” *Nano letters*, vol. 9, no. 4, pp. 1593–1597, 2009.

[45] X. Li, W. Cai, J. An, S. Kim, J. Nah, D. Yang, R. Piner, A. Velamakanni, I. Jung, E. Tutuc, S. K. Banerjee, L. Colombo, and R. S. Ruoff, “Large-Area Synthesis of High-Quality and Uniform Graphene Films on Copper Foils,” *Science*, vol. 324, no. 5932, pp. 1312–1314, 2009.

[46] Z. Sun, Z. Yan, J. Yao, E. Beitler, Y. Zhu, and J. Tour, “Growth of graphene from solid carbon sources,” *Nature*, vol. 468, no. 7323, pp. 549–555, 2010.

[47] K. S. Kim, Y. Zhao, H. Jang, S. Y. Lee, J. M. Kim, , J. H. Ahn, P. Kim, J. Y. Choi, and B. H. Hong, “Large-scale pattern growth of graphene films for stretchable transparent electrodes,” *Nature*, vol. 457, pp. 706–710, 2009.

[48] A. Reina, X. Jia, J. Ho, D. Nezich, H. Son, V. Bulovic, M. Dresselhaus, and J. Kong, “Large area, few-layer graphene films on arbitrary substrates by chemical vapor deposition,” *Nano letters*, vol. 9, no. 1, pp. 30–35, 2008.

[49] C. N. R. Rao, K. S. Subrahmanyam, H. S. S. R. Matte, B. Abdulhakeem, A. Govindaraj, B. Das, P. Kumar, A. Ghosh, and D. J. Late, “A study of the synthetic methods and properties of graphenes,” *Science and Technology of Advanced Materials*, vol. 11, no. 5, p. 054502, 2010.

[50] P. Blake, E. W. Hill, A. H. C. Neto, K. S. Novoselov, D. Jiang, R. Yang, T. J. Booth, and A. K. Geim, “Making graphene visible,” *Applied Physics Letters*, vol. 91, no. 6, pp. 1–3, 2007.

[51] G. Binnig, C. Quate, and C. Gerber, “Atomic force microscope,” *Physical review letters*, vol. 56, no. 9, pp. 930–933, 1986.

[52] C. Soldano, A. Mahmood, and E. Dujardin, “Production, properties and potential of graphene,” *Carbon*, vol. 48, no. 8, pp. 2127–2150, 2010.

[53] D. Schroder, *Semiconductor material and device characterization.* Wiley-IEEE Press, 2006.

[54] D. Graf, F. Molitor, K. Ensslin, C. Stampfer, A. Jungen, C. Hierold, and L. Wirtzs, “Spatially resolved raman spectroscopy of single-and few-layer graphene,” *Nano Lett*, vol. 7, no. 2, pp. 238–242, 2007.

[55] A. Ferrari, J. Meyer, V. Scardaci, C. Casiraghi, M. Lazzeri, F. Mauri, S. Piscanec, D. Jiang, K. Novoselov, and S. Roth, “Raman spectrum of graphene and graphene layers,” *Physical review letters*, vol. 97, no. 18, pp. 1–4, 2006.

[56] R. Vidano, “Observation of raman band shifting with excitation wavelength for carbons and graphites,” *Solid State Communications*, vol. 39, pp. 341–344, 1981.

[57] P. Raichoudhury, Ed., *SPIE Handbook of Microlithography, Micromachining and Microfabrication.* SPIE, 1998, vol. 1.

[58] I. Haller, "High-resolution positive resists for electron-beam exposure," *IBM Journal of Research and Development*, vol. 12, no. 3, pp. 251–256, 1968.

[59] J. Virtanen, "Specific contact resistivity of metal-graphene -junctions," Master's thesis, Helsinki University of Technology, May 2009.

[60] S. Fransilla, *Introduction to Microfabrication.* John Wiley and Sons Ltd, 2004.

[61] L. Campos, V. Manfrinato, J. Sanchez-Yamagishi, J. Kong, and P. Jarillo-Herrero, "Anisotropic etching and nanoribbon formation in single-layer graphene," *Nano Lett*, vol. 9, no. 7, pp. 2600–2604, 2009.

[62] X. Lu, H. Huang, N. Nemchuk, and R. Ruoff, "Patterning of highly oriented pyrolytic graphite by oxygen plasma etching," *Applied Physics Letters*, vol. 75, pp. 193 – 195, 1999.

[63] L. Liu, S. Ryu, M. R. Tomasik, E. Stolyarova, N. Jung, M. S. Hybertsen, M. L. Steigerwald, L. E. Brus, and G. W. Flynn, "Graphene oxidation: Thickness-dependent etching and strong chemical doping," *Nano Letters*, vol. 8, no. 7, pp. 1965–1970, 2008.

[64] A. Nourbakhsh, M. Cantoro, A. Klekachev, F. Clemente, B. Soree, M. H. van der Veen, T. Vosch, A. Stesmans, B. Sels, and S. De Gendt, "Tuning the fermi level of sio2-supported single-layer graphene by thermal annealing," *The Journal of Physical Chemistry C*, vol. 114, no. 15, pp. 6894–6900, 2010.

[65] J. Song, T. Ko, and S. Ryu, "Raman Spectroscopy Study of Annealing-Induced Effects on Graphene Prepared by Micromechanical Exfoliation," *Bulletin of the Korean Chemical Society*, vol. 31, no. 9, p. 2679, 2010.

[66] J. Appenzeller, S. Datta, and M. Lundstrom, "Colloquium on graphene physics and devices," http://nanohub.org/resources/7180, Sep 2009.

[67] T. Jayasekera and J. W. Mintmire, "Transport in multiterminal graphene nanodevices," *Nanotechnology*, vol. 18, no. 42, p. 424033, 2007.

[68] A. Andriotis and M. Menon, "Transport properties of branched graphene nanoribbons," *Applied Physics Letters*, vol. 92, p. 042115, 2008.

[69] B. Scott and J. Leburton, "Modeling of the output and transfer characteristics of graphene field-effect transistors," *Nanotechnology, IEEE Transactions on*, no. 99, pp. 1–1, 2011.

[70] G. Zebrev, "Graphene field effect transistors: Diffusion-drift theory," *Arxiv preprint arXiv:1102.2348*, 2011.